Research Square

Preprints are preliminary reports that have not undergone peer review.
They should not be considered conclusive, used to inform clinical practice,
or referenced by the media as validated information.

The Quadratic Coefficient Moment Governs a Leading Error Channel in Palindromic Compositions with an Explicit Velocity-Dependent Kick

Jiaqi Shen

sjq111_0@sina.com.cn

United World Colledge, Chang Shu, China https://orcid.org/0009-0009-6763-6170

Research Article

Keywords: Palindromic composition, velocity-Verlet, geometric integration, post-Newtonian correction, symplectic integrator, error analysis, Solar System dynamics

Posted Date: November 18th, 2026

DOI: https://doi.org/10.21203/rs.3.rs-11764012/v1

License: This work is licensed under a Creative Commons Attribution 4.0 International License.
Read Full License

Additional Declarations: The authors declare no competing interests.

The Quadratic Coefficient Moment Governs a Leading Error Channel in Palindromic Compositions with an Explicit Velocity-Dependent Kick

Jiaqi Shen

Department of Mathematics, UWC Changshu

Abstract

Palindromic composition of a symmetric second-order velocity-Verlet kernel is a standard technique for constructing high-order geometric integrators for separable Hamiltonian systems. When a velocity-dependent perturbation is inserted explicitly into the kick evaluations, however, the resulting elementary map is no longer self-adjoint and generically acquires a local defect of order $\mathcal{O}(\tau^2)$, where τ is the sub-step length. We show, by a Taylor expansion followed by an explicit propagation of the stage defects through the exact flow, that the leading velocity-dependent contribution to the local error of a composition is

$$H^2 Q\, d(y_0) + \mathcal{O}(H^3), \qquad Q = \sum_{i=1}^{s} w_i^2,$$

where H is the macro-step, s is the number of stages, $\{w_i\}$ are the composition weights summing to one, $y_0 = (q_0, p_0)$ denotes the initial state, and $d(y_0)$ is the leading local defect vector evaluated at the initial state. For fixed final time T, the corresponding leading global contribution is $HQ\,\eta_T(y_0) + \mathcal{O}(H^2)$, where η_T is the transported defect coefficient. Thus Q, rather than the nominal order of the separable-kernel composition, governs a leading error channel introduced by this explicit velocity-dependent treatment.

The mechanism is examined in a 28-body Solar System model containing Newtonian gravity, solar and terrestrial J_2 terms, and a Schwarzschild-type first-order post-Newtonian correction. In a one-year same-model test, a 3-minute equal-step calculation is used as a fine reference and four 30-minute compositions are compared. After accounting for the nonzero leading defect of the reference, the normalised Mercury errors of the constrained 63-stage, constrained 127-stage, and formally 10th-order 35-stage schemes agree within 0.5%. The equal-step 63-stage scheme, although it minimises Q, does not follow the same normalised relation at this time scale, indicating that uncancelled conservative and mixed next-order terms are no longer negligible. Centennial comparisons with JPL DE440 provide an independent model-consistency indication, with the equal-step scheme reducing the Mercury discrepancy from 5.64×10^{-5} to 4.26×10^{-6} AU. Controlled fixed-15-stage families spanning ranges of Q and S_3 show that the Mercury error scales with Q ($R^2 > 0.998$ for each Cartesian component) and that the error vectors remain collinear to within 0.99996. An exact linear benchmark confirms the reversal of accuracy ranking between conservative and velocity-dependent regimes, with error ratios consistent with the Q ratios.

Keywords: Palindromic composition velocity-Verlet geometric integration post-Newtonian correction symplectic integrator error analysis Solar System dynamics

1 Introduction

This work originated from an attempt to construct a first-principles long-term Solar System simulator. The study of the Solar System's long-term dynamics, including its chaotic behaviour and the stability of planetary orbits over billion-year timescales, imposes stringent demands on the accuracy and long-time structural behaviour of numerical integrators [8, 20, 17]. Using a 28-body model that included a post-Newtonian (1PN) relativistic correction, we designed a 63-stage palindromic composition whose coefficients were tuned to cancel the odd-order error moments $S_3, S_5, \ldots, S_{11}$ of the separable kernel. The expectation, based on classical order theory, was that this high-order composition would outperform simpler integrators. However, during validation against the JPL DE440 ephemeris, a striking anomaly emerged: a naive equal-step composition with $w_i = 1/63$ produced a Mercury position discrepancy more than an order of magnitude smaller than our carefully constructed 63-stage scheme. An exploratory 127-stage set satisfying the same moment constraints showed no improvement, while a formally 10th-order product-formula composition performed worst of all.

This reversal of the expected accuracy ranking motivated a detailed analysis of the error structure when a velocity-dependent force is inserted explicitly into a palindromic composition. The classical theory of symplectic integrators based on palindromic composition of the second-order leapfrog (velocity Verlet) map is well established for separable Hamiltonians [21, 4, 11, 18, 2]. For a purely position-dependent force, a palindromic coefficient set $\{w_i\}$ with $\sum w_i = 1$ and $w_{s+1-i} = w_i$ defines a method whose formal order can be raised by imposing additional moment constraints $S_k \equiv \sum_i w_i^k = 0$ for appropriate odd k. The condition $S_3 = 0$ is sufficient to eliminate the leading odd-order error term of a symmetric second-order kernel, yielding a formally fourth-order method; higher orders require additional independent constraints beyond simple power moments. General composition theory also describes how leading defects of lower-order basic maps are inherited under scaled composition, including constructions based on first-order methods and their adjoints [2]. The issue considered here is more specific: a coefficient sequence designed for a symmetric second-order separable kernel is applied to an implemented elementary map whose explicitly evaluated velocity-dependent part activates a different, uncancelled defect channel.

In many practical applications, however, the force model contains small velocity-dependent corrections that are not derived from the same separable potential. Examples include post-Newtonian (1PN) relativistic corrections used in Solar System dynamics and ephemerides [3, 17, 19], Lorentz-type forces, the Poynting–Robertson effect [16], and phenomenological drag terms. A common pragmatic approach is to evaluate these extra accelerations explicitly at the current state and insert them into the kick steps of the leapfrog formula, leaving the palindromic coefficient structure formally unchanged. This treatment breaks the self-adjointness of the elementary map and generically reduces its global accuracy to first order.

Velocity-dependent forces are known to require special care in leapfrog-type integration. Algorithmic-regularisation and auxiliary-velocity constructions have been developed for velocity-dependent few-body perturbations [12, 6], while specialised splitting methods avoid the poor behaviour of a naive leapfrog in systems with velocity-dependent Coriolis forces [15]. For inseparable Hamiltonians, extended-phase-space formulations provide explicit leapfrog-like and higher-order symmetric alternatives by enlarging the phase space and introducing mixing or projection maps [14, 10]. Recent spectral-deferred-correction analysis using velocity Verlet as the base method likewise shows that velocity dependence changes the attainable order-increase mechanism [1]. These approaches modify, symmetrise, or iteratively correct the integrator. The present work is complementary: it diagnoses the leading error channel that remains when the velocity-dependent term is inserted directly into the kick evaluations of the original Verlet-like map.

When such a perturbed elementary map is used inside a high-order composition, the global error inherits contributions both from the truncation error of the unperturbed kernel and from the discretisation of the velocity-dependent perturbation. The classical order conditions of the separable kernel do not by themselves quantify this trade-off, so a coefficient sequence optimised for the conservative subsystem need not remain optimal for the implemented full map.

In this paper we analyse this phenomenon and distinguish the leading perturbation-induced error from the total error of the composed method. The relevant coefficient quantity is

$$Q \equiv \sum_{i=1}^{s} w_i^2.$$

We prove (Proposition 1) that, for an elementary map whose velocity-dependent force is evaluated explicitly, the leading velocity-dependent contribution to the local defect of the composition is $H^2 Q\, d(y_0)$. We then derive a fixed-time global expansion in which the corresponding contribution is $HQ\, \eta_T(y_0)$. By Cauchy's inequality, the equal-step choice $w_i = 1/s$ achieves the minimum possible Q for a fixed number of stages. This minimises the leading perturbation-induced contribution, but it does not necessarily minimise the total error because the conservative-kernel error is not simultaneously cancelled.

Two complementary numerical tests are used. First, centennial discrepancies relative to JPL DE440 provide an external ephemeris benchmark and show the practical effect of changing Q. Second, a one-year same-model experiment uses an equal-step 63-stage calculation with a 3-minute macro-step as a fine reference. For the constrained 63-stage, constrained 127-stage, and Morales 35-stage schemes, all run with a 30-minute macro-step, the Mercury errors normalised by the reference-corrected coefficient $Q - (H_{\mathrm{ref}}/H)Q_{\mathrm{ref}}$ agree within 0.5%. The equal-step 30-minute calculation does not follow this same line at one year because, once its Q-dependent term has been strongly reduced, uncancelled conservative and other $\mathcal{O}(H^2)$ contributions are no longer negligible. This contrast is consistent with competition between the two error channels. These results are complemented by controlled 15-stage families and an exact linear benchmark (Sections 4.6 and 4.7).

The remainder of the paper is structured as follows. Section 2 describes the physical model and the integrator. Section 3 presents the local and global error analysis. Section 4 reports the numerical experiments. Section 5 discusses the implications for integrator design, and Section 6 concludes.

2 Physical Model and Integrator

2.1 Reference system and force model

We consider a 28-body model of the Solar System consisting of the Sun, the eight planets, Pluto, the Moon, Eris, and 16 main-belt asteroids. The equations of motion are formulated in the J2000.0 mean ecliptic frame with origin at the Solar System barycentre. The unit system uses the solar mass $M_\odot$ as the mass unit, the astronomical unit (AU) as the length unit, and a derived time unit (TU) such that $GM_\odot = 1\,\mathrm{AU}^3/\mathrm{TU}^2$. In these units $G = 1$ and the speed of light is $c \approx 10065.32\,\mathrm{AU/TU}$. Initial conditions are taken from JPL HORIZONS at epoch JD 2461185.5; the gravitational parameters GM of all bodies are adopted from DE440 [3, 7].

The total force on each body is the sum of:

- Newtonian gravity, computed in the absolute frame with exact enforcement of Newton's third law.
- A first-order post-Newtonian (1PN) Schwarzschild-type correction, representing the dominant solar relativistic contribution in a test-particle approximation [19], applied to every Sun–body pair. The acceleration of body i relative to the Sun is

$$\mathbf{a}_{1\mathrm{PN},i} = \frac{GM_\odot}{c^2 r_i^3}\Big[\big(\tfrac{4GM_\odot}{r_i} - v_i^2\big)\mathbf{r}_i + 4(\mathbf{r}_i \cdot \mathbf{v}_i)\mathbf{v}_i\Big], \tag{1}$$

  where $\mathbf{r}_i = \mathbf{r}_i^{\mathrm{SSB}} - \mathbf{r}_\odot^{\mathrm{SSB}}$, $r_i = \|\mathbf{r}_i\|$, and $\mathbf{v}_i$ is the relative velocity with $v_i^2 = \mathbf{v}_i \cdot \mathbf{v}_i$. The force $\mathbf{F}_i^{1\mathrm{PN}} = m_i \mathbf{a}_{1\mathrm{PN},i}$ is applied to body i; the negative sum of all such forces is applied to the Sun.
- Zonal harmonic J_2 perturbations of the Sun (on all orbiting bodies) and of the Earth (on the Moon only). The Earth's spin axis is updated once per model year using the 24-term Fourier expansion of Laskar et al. [9].

No inter-body 1PN terms are included; the adopted model is a test-particle-type Sun–body approximation supplemented by momentum-balancing reactions on the Sun, and is not intended to represent the full Einstein–Infeld–Hoffmann equations.

2.2 Elementary kick–drift–kick map and palindromic composition

Within each one-year interval the Earth's spin axis is held fixed, so the position-dependent part of the force is autonomous and separable,

$$H_0(\mathbf{q}, \mathbf{p}) = T(\mathbf{p}) + V(\mathbf{q}).$$

We apply the usual velocity-Verlet kick–drift–kick formula

$$\begin{aligned} \mathbf{p}_{n+1/2} &= \mathbf{p}_n + \frac{\tau}{2}\mathbf{F}(\mathbf{q}_n, \mathbf{p}_n), \\ \mathbf{q}_{n+1} &= \mathbf{q}_n + \tau\, M^{-1}\mathbf{p}_{n+1/2}, \\ \mathbf{p}_{n+1} &= \mathbf{p}_{n+1/2} + \frac{\tau}{2}\mathbf{F}(\mathbf{q}_{n+1}, \mathbf{p}_{n+1/2}), \end{aligned} \tag{2}$$

where $\mathbf{F} = \mathbf{F}_{\mathrm{Newton}} + \mathbf{F}_{J_2} + \mathbf{F}_{1\mathrm{PN}}$ and τ denotes the sub-step length. We denote this map by Φ_τ.

For a purely position-dependent force, Φ_τ is the standard velocity-Verlet map and is symmetric, symplectic, and globally second-order accurate. When $\mathbf{F}$ depends on velocity, the two kicks are evaluated with different momenta ($\mathbf{p}_n$ and $\mathbf{p}_{n+1/2}$); the resulting Verlet-like map is no longer self-adjoint and generically reduces the global accuracy to first order (see Section 3). This loss of the standard leapfrog properties in the presence of velocity-dependent forces is consistent with earlier analyses and specialised constructions for such systems [12, 6, 15, 1].

A palindromic composition of length s is defined by a set of real coefficients $\{w_i\}_{i=1}^{s}$ satisfying $\sum_i w_i = 1$ and $w_{s+1-i} = w_i$. One macro-step of size H is

$$\Psi_H^{(w)} = \Phi_{w_s H} \circ \cdots \circ \Phi_{w_1 H}.$$

For the production runs we use $s = 63$ and $H = 0.5\,\mathrm{h} \approx 3.58 \times 10^{-4}\,\mathrm{TU}$.

2.3 Coefficient sets

We compare four choices of $\{w_i\}$:

1. **63-stage constrained** — obtained by solving $S_1 = 1$, $S_3 = S_5 = \cdots = S_{11} = 0$. The coefficients are mostly positive and of comparable magnitude (see Appendix A).
2. **Equal-step 63-stage** — $w_i = 1/63$ for all i.
3. **127-stage constrained** — satisfying the same odd-order moment constraints (Appendix A).
4. **Morales 35-stage** — a 35-stage palindromic set from Table III of Morales et al. [13], corresponding to a formally 10th-order product formula for a separable Hamiltonian. Although originally developed for quantum product formulas, the coefficient sequence satisfies the algebraic composition conditions required for a classical separable Hamiltonian.

For a generic symmetric second-order separable kernel, $S_3 = 0$ makes the constrained 63-stage and 127-stage compositions formally fourth order. The additional conditions $S_5 = \cdots = S_{11} = 0$ are extra vanishing power moments; by themselves they do not establish an order above four.

All methods use the same macro-step $H = 0.5\,\mathrm{h}$. The 63-stage sets require 126 force evaluations per macro-step, the Morales set requires 70, and the 127-stage set requires 254. These cost differences must be kept in mind when interpreting the results: the comparisons at fixed H reveal the error-coefficient mechanism, but a cost-normalised comparison would require adjusting the macro-step so that all methods perform the same number of force evaluations per unit time.

3 Error analysis for the explicitly perturbed kernel

3.1 Local error of the elementary map

Consider the map (2) with a small step τ. In the composition, each sub-step has length $\tau = w_i H$ for some weight w_i, but for the elementary analysis τ can be regarded as a generic small parameter. Write

$v = M^{-1}p$ and $F = F(q,p)$. Here F_q and F_p denote the Jacobian matrices of F with respect to q and p, respectively, and all derivatives are evaluated at (q_n, p_n).

The exact solution over an interval τ satisfies

$$q(t+\tau) = q + \tau v + \frac{\tau^2}{2} M^{-1} F + \mathcal{O}(\tau^3),$$

$$p(t+\tau) = p + \tau F + \frac{\tau^2}{2}\big(F_q v + F_p F\big) + \mathcal{O}(\tau^3).$$

For the numerical map,

$$p^* = p + \frac{\tau}{2} F, \qquad q_{n+1} = q + \tau v + \frac{\tau^2}{2} M^{-1} F.$$

The force in the second kick expands as

$$F(q_{n+1}, p^*) = F + \tau F_q v + \frac{\tau}{2} F_p F + \mathcal{O}(\tau^2),$$

giving

$$p_{n+1} = p + \tau F + \frac{\tau^2}{2} F_q v + \frac{\tau^2}{4} F_p F + \mathcal{O}(\tau^3).$$

The local errors are therefore

$$q_{n+1} - q(t+\tau) = \mathcal{O}(\tau^3), \qquad p_{n+1} - p(t+\tau) = -\frac{\tau^2}{4} F_p F + \mathcal{O}(\tau^3).$$

Thus the elementary map has a leading local defect of order $\mathcal{O}(\tau^2)$ whenever $F_p F \neq 0$. The expression for the leading local error, $-\tau^2 F_p F/4$, is independent of the specific form of the velocity-dependent force; it applies to any smooth $F(q,p)$ evaluated explicitly in the kick steps. Under the standard stability assumptions used below, this produces a generically first-order global method. In the special case where the velocity-dependent force has the particular structure $F_p F = 0$ identically, the leading defect vanishes and the elementary map may retain second-order accuracy; this situation does not occur for the 1PN correction considered in the numerical experiments, nor does it affect the analysis of the velocity-dependent error channel that is the subject of this work.

3.2 Composition and propagation of the defect

Let $y = (q,p)$ and write the elementary map in the uniform local form

$$\Phi_\tau(y) = \varphi_\tau(y) + \tau^2 d(y) + R_\tau(y), \qquad \|R_\tau(y)\| \le C|\tau|^3, \tag{3}$$

where φ_τ is the exact flow of the full system and

$$d(q,p) = \begin{pmatrix} 0 \\ \\ -\frac{1}{4} F_p(q,p) F(q,p) \end{pmatrix}.$$

The vector $d(y)$ is the leading local defect of the elementary map; its only non-zero block is the momentum error $-\frac{1}{4} F_p F$. The remainder estimate is assumed uniform on a compact neighbourhood containing the exact and numerical stage values. Negative substeps are allowed; only $|\tau|$ enters the remainder bound.

For the coefficient sequence $\{w_j\}_{j=1}^{s}$, define

$$c_0 = 0, \qquad c_j = \sum_{i=1}^{j} w_i, \qquad c_s = 1.$$

The exact state at the accumulated stage time is

$$\bar{y}_j = \varphi_{c_j H}(y_0),$$

while the numerical stage values satisfy

$$y_j = \Phi_{w_j H}(y_{j-1}), \qquad y_0 = \bar{y}_0.$$

In the following, $D\varphi_t(y)$ denotes the Jacobian (state transition matrix) of the exact flow φ_t evaluated at the state y; it describes the linearised propagation of a perturbation along the exact trajectory.

Proposition 1 (Transported stage-defect expansion)**.** *Assume that the full vector field is C^3 on a compact neighbourhood of the relevant trajectory, that the exact flow and its first two variational derivatives are bounded there, and that the coefficient sequence is fixed as $H \to 0$. Then*

$$\Psi_H^{(w)}(y_0) - \varphi_H(y_0) = H^2 \sum_{j=1}^{s} w_j^2 \, D\varphi_{(1-c_j)H}(\bar{y}_j)\, d(\bar{y}_{j-1}) + \mathcal{O}(H^3) \tag{4}$$

$$= H^2 Q \, d(y_0) + \mathcal{O}(H^3), \qquad Q = \sum_{j=1}^{s} w_j^2. \tag{5}$$

The constants hidden in the remainders may depend on the fixed coefficient sequence and on bounds for the flow, but not on H.

Proof. Set $e_j = y_j - \bar{y}_j$. From (3),

$$y_j = \varphi_{w_j H}(y_{j-1}) + H^2 w_j^2 d(y_{j-1}) + \mathcal{O}(H^3),$$

where the $\mathcal{O}(H^3)$ term is uniform because the coefficients are fixed. Expanding the exact flow around $\bar{y}_{j-1}$ gives

$$\varphi_{w_j H}(y_{j-1}) = \varphi_{w_j H}(\bar{y}_{j-1}) + D\varphi_{w_j H}(\bar{y}_{j-1}) e_{j-1} + \mathcal{O}(\|e_{j-1}\|^2).$$

Since the number of stages is fixed, induction gives $e_j = \mathcal{O}(H^2)$. Hence the quadratic term above is $\mathcal{O}(H^4)$, and replacing $d(y_{j-1})$ by $d(\bar{y}_{j-1})$ changes the result only by $\mathcal{O}(H^4)$. Therefore,

$$e_j = D\varphi_{w_j H}(\bar{y}_{j-1}) e_{j-1} + H^2 w_j^2 d(\bar{y}_{j-1}) + \mathcal{O}(H^3). \tag{6}$$

Iterating (6) and using the chain rule for the exact flow yields

$$e_s = H^2 \sum_{j=1}^{s} w_j^2 \, D\varphi_{(c_s - c_j)H}(\bar{y}_j) d(\bar{y}_{j-1}) + \mathcal{O}(H^3),$$

which is (4) because $c_s = 1$. Finally,

$$D\varphi_{(1-c_j)H}(\bar{y}_j) = I + \mathcal{O}(H), \qquad d(\bar{y}_{j-1}) = d(y_0) + \mathcal{O}(H),$$

uniformly over the finite set of stages. Because $d(\bar{y}_{j-1}) = d(y_0) + \mathcal{O}(H)$, replacing each $d(\bar{y}_{j-1})$ with $d(y_0)$ introduces an additional error of $\mathcal{O}(H^3)$ which is absorbed into the remainder. Substitution gives

$$e_s = H^2 \left(\sum_{j=1}^{s} w_j^2 \right) d(y_0) + \mathcal{O}(H^3),$$

which proves (5). □

Corollary 1 (Fixed-time global expansion)**.** *Let $T > 0$ be fixed, let $N = T/H$ be an integer, and assume that the numerical orbit remains in the compact neighbourhood used in Proposition 1. Then*

$$y_N - \varphi_T(y_0) = HQ\,\eta_T(y_0) + \mathcal{O}(H^2), \tag{7}$$

where

$$\eta_T(y_0) = \int_0^T D\varphi_{T-t}(\varphi_t(y_0))\, d(\varphi_t(y_0))\; dt. \tag{8}$$

The vector $\eta_T(y_0)$ is the result of propagating the local defect d along the exact trajectory from time 0 to T; it depends only on the exact flow and the defect vector field, not on the numerical coefficients. Thus the leading perturbation-induced global error is $\mathcal{O}(HQ)$ for fixed T; no claim of simple proportionality to T is required.

Proof. Let $x_n = \varphi_{t_n}(y_0)$ with $t_n = nH$ and set $e_n = y_n - x_n$. From Proposition 1 we have the uniform one-macro-step expansion

$$\Psi_H^{(w)}(z) = \varphi_H(z) + H^2 Q\, d(z) + H^3 r_H(z),$$

where r_H is uniformly bounded on the relevant compact set. The flow is locally Lipschitz with

$$\|\varphi_H(z_1) - \varphi_H(z_2)\| \le (1 + LH)\|z_1 - z_2\|$$

for sufficiently small H. Together with the local defect bound, this gives

$$\|e_{n+1}\| \le (1 + LH)\|e_n\| + CH^2.$$

A discrete Gronwall argument [5] therefore yields

$$\max_{0 \le n \le N} \|e_n\| = \mathcal{O}(H).$$

We now refine the recurrence. Since φ_0 is the identity and the vector field is C^3, the second derivative of the short-time flow satisfies $D^2\varphi_H = \mathcal{O}(H)$ uniformly on the compact set. Expanding $\varphi_H(x_n + e_n)$ and $d(x_n + e_n)$ about x_n gives

$$e_{n+1} = D\varphi_H(x_n)e_n + H^2 Q\, d(x_n) + \mathcal{O}(H^3) + \mathcal{O}(H^2\|e_n\|) + \mathcal{O}(H\|e_n\|^2).$$

Using $\|e_n\| = \mathcal{O}(H)$, the last two terms are both $\mathcal{O}(H^3)$ uniformly for $0 \le n < N$. Hence

$$e_{n+1} = D\varphi_H(x_n)e_n + H^2 Q\, d(x_n) + \mathcal{O}(H^3).$$

Iterating this recurrence and using the chain rule for the exact flow gives

$$e_N = H^2 Q \sum_{n=0}^{N-1} D\varphi_{T-t_{n+1}}(x_{n+1})\, d(x_n) + \mathcal{O}(NH^3).$$

Since $N = T/H$, the accumulated remainder is $\mathcal{O}(H^2)$. Replacing t_{n+1} and x_{n+1} by t_n and x_n changes the sum only by another $\mathcal{O}(H^2)$ contribution. Hence

$$e_N = HQ\left[H\sum_{n=0}^{N-1} D\varphi_{T-t_n}(x_n)d(x_n)\right] + \mathcal{O}(H^2).$$

The expression in brackets is a Riemann sum for $\eta_T(y_0)$, which proves the result. □

3.3 Extension to the piecewise time-dependent model

The analysis above is stated for an autonomous vector field. In the Solar System implementation, the prescribed terrestrial spin axis is held fixed within each model year and is updated only at year boundaries. Proposition 1 therefore applies directly within each yearly segment. A multi-year expansion is obtained by composing the segment-wise error propagators, or equivalently by using the two-parameter flow of the corresponding piecewise non-autonomous system. The quadratic factor Q is unchanged; only the transported coefficient is replaced by its time-dependent analogue.

3.4 Optimality of equal coefficients

Under the consistency constraint $\sum_i w_i = 1$, Cauchy's inequality gives

$$Q = \sum_{i=1}^{s} w_i^2 \geq \frac{1}{s},$$

with equality if and only if

$$w_1 = \cdots = w_s = \frac{1}{s}.$$

Therefore the equal-step coefficients uniquely minimise the leading Q-dependent defect among real s-stage coefficient sets. Note that this result itself does not require the coefficients to be palindromic; palindromicity is relevant to the conservative-kernel design of the tested schemes.

This statement is deliberately limited. It assumes a fixed stage number, equal cost per stage, fixed real coefficients, and an asymptotic regime in which the term (7) dominates. It does not imply that the equal-step scheme minimises the total error, nor that it is optimal when stage numbers, stability restrictions, implicit solves, round-off accumulation, or the treatment of the velocity-dependent force are changed.

3.5 Competition with the conservative-kernel error

Write the force as

$$F(q,p) = F_0(q) + \varepsilon G(q,p),$$

where F_0 is position dependent, ε measures the strength of the velocity-dependent perturbation, and $G_p = \partial G/\partial p$. Since $(F_0)_p = 0$,

$$F_p F = \varepsilon G_p F_0 + \varepsilon^2 G_p G,$$

so the leading defect is $\mathcal{O}(\varepsilon)$ and generically linear in ε.

Let $w = (w_1, \ldots, w_s)$ be a fixed coefficient sequence, $N = T/H$, and $y_N^{(w,\varepsilon)}$ the numerical solution after N macro-steps. Denote the exact flow of the full system by φ_t^ε and define the fixed-time vector error by

$$e^\varepsilon(T; H, w) := y_N^{(w,\varepsilon)} - \varphi_T^\varepsilon(y_0).$$

Corollary 1 gives

$$e^\varepsilon(T; H, w) = HQ\,\eta_T^\varepsilon(y_0) + H^2\rho_T(H, w, \varepsilon; y_0), \qquad Q = \sum_{i=1}^{s} w_i^2, \tag{9}$$

where η_T^ε is the transported defect coefficient defined in Corollary 1, evaluated for the force $F_0 + \varepsilon G$, and $\eta_T^\varepsilon(y_0) = \mathcal{O}(\varepsilon)$ as $\varepsilon \to 0$. The remainder term $\rho_T(H, w, \varepsilon; y_0)$ is defined by

$$H^2\rho_T(H, w, \varepsilon; y_0) := e^\varepsilon(T; H, w) - HQ\,\eta_T^\varepsilon(y_0),$$

so that ρ_T absorbs exactly the $\mathcal{O}(H^2)$ remainder in Corollary 1. For fixed T and a fixed coefficient sequence, $\rho_T(H, w, \varepsilon; y_0)$ remains bounded as $H \to 0$ and contains the conservative, higher-order velocity-dependent, and mixed contributions. Equation (9) is a vector decomposition and does not imply additivity of error norms.

In the conservative limit $\varepsilon = 0$, the elementary map reduces to the symmetric second-order velocity-Verlet kernel. Classical symmetric-composition theory [4, 11, 21] yields the formal fixed-time expansion

$$e^0(T; H, w) = H^2 S_3\,\zeta_{3,T}(y_0) + \mathcal{O}(H^4), \qquad S_3 := \sum_{i=1}^{s} w_i^3. \tag{10}$$

Here $\zeta_{3,T}$ depends on the conservative problem, the initial state, the integration time, and the underlying Verlet kernel, but not on the composition weights. The $\mathcal{O}(H^4)$ terms involve several independent commutator structures and are not determined by S_5 alone. Thus $S_3 = 0$ removes the leading conservative contribution but does not by itself guarantee an order above four.

A composition with $S_3 = 0$ cannot be the equal-step sequence and therefore has $Q > 1/s$, often substantially larger. Conversely, equal steps minimize $Q = 1/s$ but leave $S_3 = 1/s^2 \neq 0$. The numerical accuracy therefore reflects a crossover between the HQ velocity-dependent channel and the H^2S_3 conservative channel. At fixed H and T, a moment-cancelling composition can be superior when the conservative contribution dominates, whereas the error ordering is governed primarily by Q when the explicitly discretised velocity-dependent term dominates.

4 Numerical experiments

4.1 Setup and DE440 model-consistency check

All integrations start from JD 2461185.5 and run for 100 model years (36 500 days). The final state is compared with JPL DE440 [3]. Because DE440 uses a different force model, the differences represent a model-consistency check rather than a strict numerical error measurement. Nevertheless, under identical physical models and step sizes, the relative performance ranking of the integrators reflects the influence of the numerical scheme. The DE440 benchmark is not intended to measure the pure truncation error of

the discretisation; instead, it provides an external reference under a fixed model difference. The observed proportionality between position discrepancies and Q is therefore consistent with the Q-dependent error being the dominant *variable* component among the tested integrators for the inner planets.

Table 1 lists the position discrepancies for all bodies, and Table 2 displays Q together with the Mercury discrepancy.

Table 1: Centennial position discrepancies relative to JPL DE440 (macro-step 0.5 h).

Body	63-stage	Eq.-step 63	127-stage	Morales 35
Mercury	5.64×10^{-5}	4.26×10^{-6}	8.18×10^{-5}	7.45×10^{-4}
Venus	1.87×10^{-6}	1.64×10^{-7}	2.78×10^{-6}	2.66×10^{-5}
Earth	5.99×10^{-7}	2.46×10^{-7}	8.03×10^{-7}	6.32×10^{-6}
Moon	2.21×10^{-6}	2.39×10^{-6}	2.17×10^{-6}	6.29×10^{-6}
Mars	2.91×10^{-7}	2.48×10^{-7}	3.16×10^{-7}	1.15×10^{-6}
Jupiter	2.48×10^{-7}	2.48×10^{-7}	2.50×10^{-7}	2.50×10^{-7}
Saturn	1.78×10^{-7}	1.79×10^{-7}	1.79×10^{-7}	1.79×10^{-7}
Uranus	7.26×10^{-7}	7.27×10^{-7}	7.26×10^{-7}	7.26×10^{-7}
Neptune	5.86×10^{-6}	5.86×10^{-6}	5.86×10^{-6}	5.86×10^{-6}
Pluto	6.40×10^{-6}	6.40×10^{-6}	6.40×10^{-6}	6.40×10^{-6}

Table 2: Quadratic coefficient moment Q and centennial Mercury discrepancy.

Scheme	Stages s	Q	Mercury discr. (AU)	Ratio to 63-stage
Eq.-step 63	63	0.01587	4.26×10^{-6}	0.076
63-stage	63	0.22689	5.64×10^{-5}	1.000
127-stage	127	0.32910	8.18×10^{-5}	1.450
Morales 35	35	2.99571	7.45×10^{-4}	13.21

The ratios of the Mercury discrepancies track the ratios of Q to within a few percent:

$$\frac{Q_{127}}{Q_{63}} = 1.450, \quad \frac{E_{127}}{E_{63}} = 1.450; \qquad \frac{Q_{\mathrm{M35}}}{Q_{63}} = 13.20, \quad \frac{E_{\mathrm{M35}}}{E_{63}} = 13.21.$$

The equal-step scheme reduces the discrepancy by a factor of 13.24 compared with the 63-stage set, while the ratio of their Q values is 14.29. Figure 1 juxtaposes this centennial DE440 benchmark with the one-year same-model comparison introduced in Section 4.2.

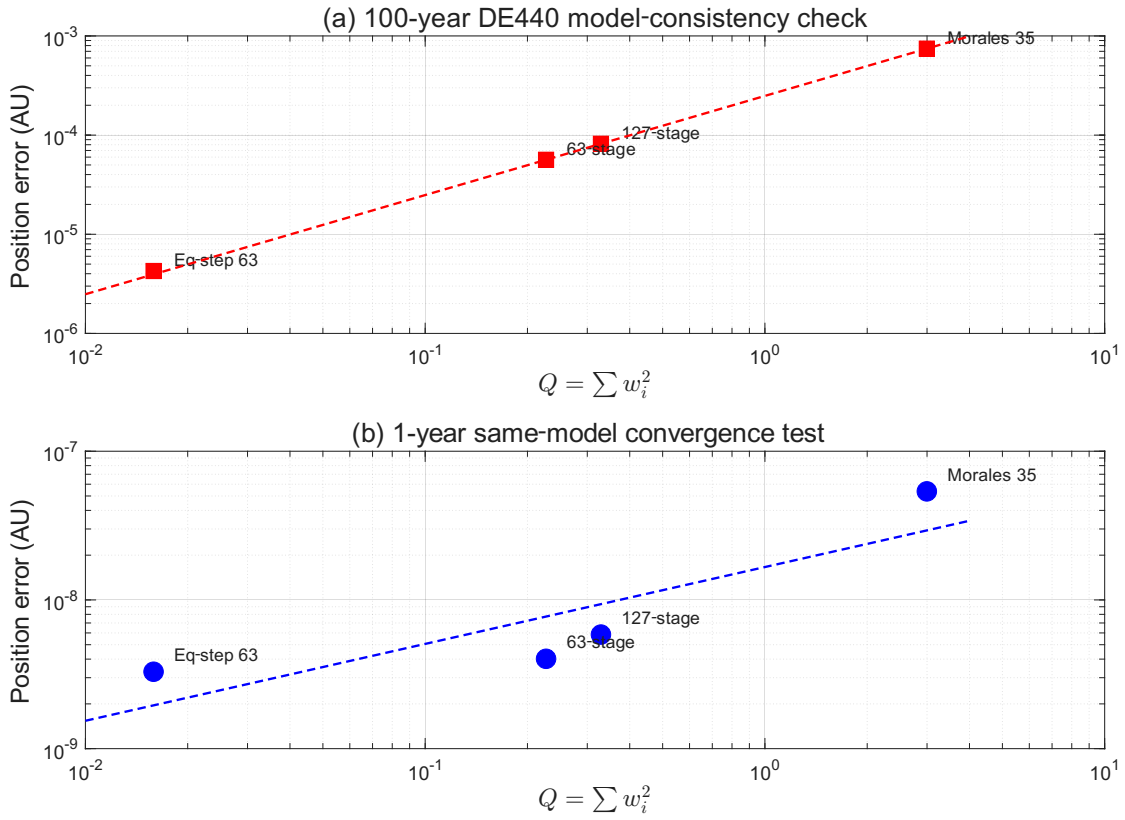


Figure 1: Mercury position difference versus the quadratic coefficient moment $Q = \sum_i w_i^2$ for the four tested compositions. (a) Centennial discrepancy relative to JPL DE440, used as an external model-consistency benchmark. (b) One-year same-model position difference relative to the equal-step 63-stage reference with $H_{\mathrm{ref}} = 3\,\mathrm{min}$; all four tested calculations use $H = 30\,\mathrm{min}$. The dashed lines are visual linear guides. Panel (a) shows the practical ephemeris consequence of changing Q under a fixed model difference, while panel (b) removes the DE440 force-model offset and directly compares the discretisations of the adopted equations.

For the outer planets the DE440 discrepancies are essentially independent of the integration scheme, indicating that they are limited mainly by force-model differences at the displayed scale. For Mercury and Venus, the discrepancy ordering closely follows Q. Panel (b) of Figure 1 provides the complementary same-model comparison; the reference correction and the residual conservative-kernel contribution are analysed below.

4.2 One-year same-model reference experiment

To separate discretisation error from the force-model difference contained in the DE440 comparison, all four compositions were integrated for one model year using exactly the same 28-body equations and initial state. The tested macro-step was

$$H = 30\,\mathrm{min}.$$

A finer calculation using the equal-step 63-stage scheme with

$$H_{\mathrm{ref}} = 3\,\mathrm{min}$$

was used as the common reference. Thus the reference uses the same elementary map but ten times the number of macro-steps. For each body B, the reported quantity is

$$E_B^{(w)} = \left\| \mathbf{r}_{B,H}^{(w)}(T) - \mathbf{r}_{B,H_{\mathrm{ref}}}^{(\mathrm{ref})}(T) \right\|_2 .$$

Table 3 gives these Euclidean position differences at the one-year endpoint; the corresponding Mercury values are plotted in Figure 1(b).

Table 3: One-year same-model position errors relative to the equal-step 63-stage reference with $H_{\mathrm{ref}} = 3\,\mathrm{min}$. All tested methods use $H = 30\,\mathrm{min}$.

Body	Eq.-step 63	Constrained 63	Constrained 127	Morales 35
Mercury	3.294915×10^{-9}	4.024280×10^{-9}	5.854039×10^{-9}	5.373979×10^{-8}
Venus	2.446489×10^{-10}	1.921112×10^{-10}	2.804420×10^{-10}	2.596216×10^{-9}
Earth	6.542260×10^{-11}	4.674054×10^{-11}	6.739854×10^{-11}	6.142637×10^{-10}
Moon	4.179874×10^{-10}	3.365295×10^{-11}	5.338401×10^{-11}	7.764541×10^{-10}
Mars	2.444314×10^{-11}	9.494722×10^{-12}	1.005988×10^{-11}	7.410439×10^{-11}
Jupiter	1.436989×10^{-12}	1.701862×10^{-12}	1.084132×10^{-12}	1.683741×10^{-12}
Saturn	1.048343×10^{-11}	1.100406×10^{-11}	9.177018×10^{-12}	1.120007×10^{-11}
Uranus	2.112679×10^{-12}	8.192319×10^{-13}	1.792771×10^{-12}	9.704166×10^{-13}
Neptune	4.372123×10^{-13}	1.141417×10^{-12}	8.113641×10^{-13}	2.580724×10^{-12}
Pluto	7.063236×10^{-12}	2.364838×10^{-12}	2.080385×10^{-12}	3.217131×10^{-12}

The fine reference is not an exact solution and retains its own leading Q-dependent defect. Corollary 1 predicts, for a tested method w,

$$y_H^{(w)}(T) - y_{H_{\mathrm{ref}}}^{(\mathrm{ref})}(T) = (HQ_w - H_{\mathrm{ref}}Q_{\mathrm{ref}})\,\eta_T + \mathcal{R}_w, \tag{11}$$

where $\mathcal{R}_w$ contains the conservative-kernel and mixed contributions, together with terms of order $\mathcal{O}(H^2)+\mathcal{O}(H_{\mathrm{ref}}^2)$ for fixed T. The leading factor $HQ_w - H_{\mathrm{ref}}Q_{\mathrm{ref}}$ reflects the fact that the reference solution itself carries a Q-dependent defect proportional to $H_{\mathrm{ref}}Q_{\mathrm{ref}}$. Without this correction, the normalised errors would carry an offset proportional to $H_{\mathrm{ref}}Q_{\mathrm{ref}}/\widehat{Q}_w$, which is non-negligible for the smaller Q values. Since $H_{\mathrm{ref}}/H = 0.1$ and

$$Q_{\mathrm{ref}} = Q_{\mathrm{eq}} = \frac{1}{63},$$

the reference-corrected quadratic moment is

$$\widehat{Q}_w = Q_w - \frac{H_{\mathrm{ref}}}{H}Q_{\mathrm{ref}} = Q_w - \frac{1}{630}. \tag{12}$$

Table 4 shows the normalised errors. For Mercury, the constrained 63-stage, constrained 127-stage, and Morales 35-stage values of $E/\widehat{Q}$ agree within 0.5%. The same spread is approximately 1.7% for Venus and 1.1% for Earth.

Table 4: Reference-corrected quadratic moments and normalised one-year same-model errors. The normalisation is diagnostic of the leading Q-dependent channel and is not expected to collapse methods whose conservative-kernel error is comparable.

Scheme	Q	$\widehat{Q}$	$E_{\mathrm{Mercury}}/\widehat{Q}$	$E_{\mathrm{Venus}}/\widehat{Q}$	$E_{\mathrm{Earth}}/\widehat{Q}$
Eq.-step 63	0.0158730	0.0142857	2.30644×10^{-7}	1.71254×10^{-8}	4.57958×10^{-9}
Constrained 63	0.2268875	0.2253002	1.78619×10^{-8}	8.52690×10^{-10}	2.07459×10^{-10}
Constrained 127	0.3290986	0.3275113	1.78743×10^{-8}	8.56282×10^{-10}	2.05790×10^{-10}
Morales 35	2.9957134	2.9941261	1.79484×10^{-8}	8.67103×10^{-10}	2.05156×10^{-10}

The ratio test avoids fitting an intercept. For Mercury,

$$\frac{\widehat{Q}_{127}}{\widehat{Q}_{63}} = 1.453666, \qquad \frac{E_{127}}{E_{63}} = 1.454680,$$

a relative difference of 0.070%. Likewise,

$$\frac{\widehat{Q}_{\mathrm{M35}}}{\widehat{Q}_{63}} = 13.289495, \qquad \frac{E_{\mathrm{M35}}}{E_{63}} = 13.353889,$$

a relative difference of 0.485%. These results provide strong same-model evidence consistent with the prediction that the leading error of the three high-order conservative compositions is proportional to Q at the tested step and interval.

The equal-step 30-minute scheme does not lie on the same normalised line at one year. This is not a contradiction of the theory. Equal steps minimise the perturbation defect, but they do not cancel the conservative third-order local error: $S_3 = 1/63^2$. Once the Q-dependent term has been strongly reduced, the remaining conservative and mixed $\mathcal{O}(H^2)$ contributions are no longer negligible. The Moon provides an especially clear indication of a different error balance: its rapid Earth–Moon dynamics are consistent with the constrained 63-stage scheme benefiting from its conservative-kernel cancellations at this time scale. Conversely, the centennial DE440 result for Mercury is consistent with the smaller Q of the equal-step method becoming the dominant practical advantage over the longer interval.

The normalised Mercury signal is approximately 21 times that of Venus and 87 times that of Earth. Therefore, residual terms of a comparable absolute scale would cause a larger relative spread in the Venus and Earth ratios. This is a plausible explanation for the observed differences, but it is not yet an isolated error-budget measurement. The 3-minute calculation is not treated as exact; future work could refine the reference solution and provide vector-error analyses.

4.3 DE440 control with 1PN and Earth-J_2 disabled

As a physical-model control, we repeated the 100-year integration with both the 1PN correction and the Earth-J_2 perturbation disabled, leaving an autonomous Newtonian-plus-solar-J_2 model. The results are listed in Table 5. This experiment is not used to measure the order of the conservative integrators, because the omitted relativistic acceleration dominates the comparison with DE440.

Table 5: DE440 discrepancies for the autonomous Newtonian-plus-solar-J_2 control model, with 1PN and Earth J_2 disabled.

Body	63-stage constrained	Eq.-step 63
Mercury	3.79×10^{-4}	3.79×10^{-4}
Venus	6.12×10^{-5}	6.12×10^{-5}
Earth	3.50×10^{-5}	3.50×10^{-5}
Mars	2.62×10^{-5}	2.62×10^{-5}
Jupiter	2.78×10^{-6}	2.78×10^{-6}
Saturn	1.20×10^{-6}	1.19×10^{-6}

The two schemes produce nearly identical results for all planets. This near-equality is a consequence of the missing 1PN acceleration: without it, the dominant source of discrepancy with DE440 is the absent relativistic perihelion advance ($\sim 43''$ per century for Mercury) [19], which is a model deficiency rather than a numerical error. Resolving the small numerical differences between the two integrators in the purely conservative setting would require a same-model convergence test with a high-accuracy reference solution.

The long-term energy behaviour in this autonomous control (Figure 2) shows that the monitored Newtonian-plus-solar-J_2 energy, defined as

$$E_{\mathrm{mon}} = \sum_i \frac{\mathbf{p}_i^2}{2m_i} - \sum_{i<j} \frac{Gm_i m_j}{r_{ij}} + V_{J_2}^{\odot},$$

remains bounded at the 10^{-12} level with no detectable secular drift over 1000 years, providing a long-time structural check. Bounded energy oscillation is also shared by many symplectic and symmetric methods and does not by itself determine the order of accuracy.

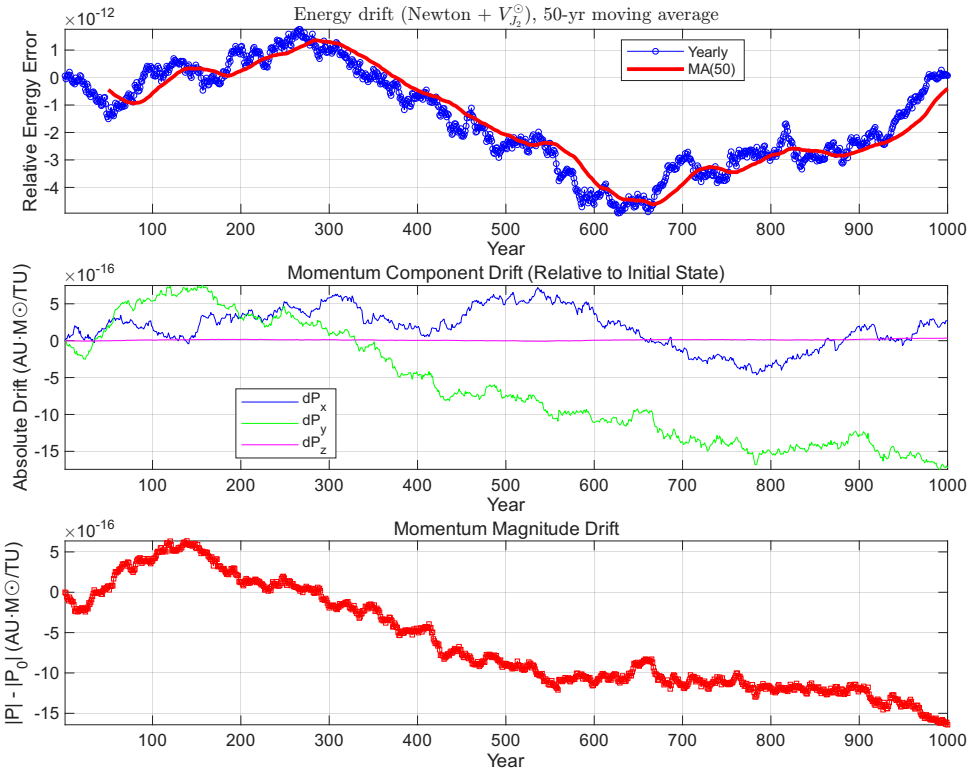


Figure 2: Energy and momentum diagnostics for the constrained 63-stage integrator in the autonomous Newtonian-plus-solar-J_2 control model, with 1PN and Earth J_2 disabled.

4.4 Long-term behaviour with 1PN

The energy diagnostics reported here serve as code-consistency and long-term stability checks; they are not intended as direct validations of the Q-scaling law. When the 1PN correction is activated, the monitored Newtonian-plus-solar-J_2 energy develops a slow linear drift, as shown in Figure 3 for the 63-stage constrained set. The 50-year moving average reaches a relative offset of 1.79×10^{-9} after 1000 years. Barycentric momentum remains at the round-off level, as expected from the explicit force balancing.

A 100,000-year integration of the same 63-stage set with a barycentre-merged 27-body diagnostic (Appendix B) shows a continuation of this trend at an approximately constant slope. The 27-body reduction was used to reduce storage requirements while preserving the secular information of the planetary orbits. No numerical blow-up or systematic momentum leakage was observed in that run.

We caution that the monitored quantity excludes both the 1PN and Earth-J_2 contributions and is not a conserved invariant of the implemented model; its drift reflects omitted physical contributions and numerical discretisation effects in unknown proportions. The energy diagnostic should therefore be regarded as a code-consistency and long-term stability check rather than as a validation of the Q-scaling law.

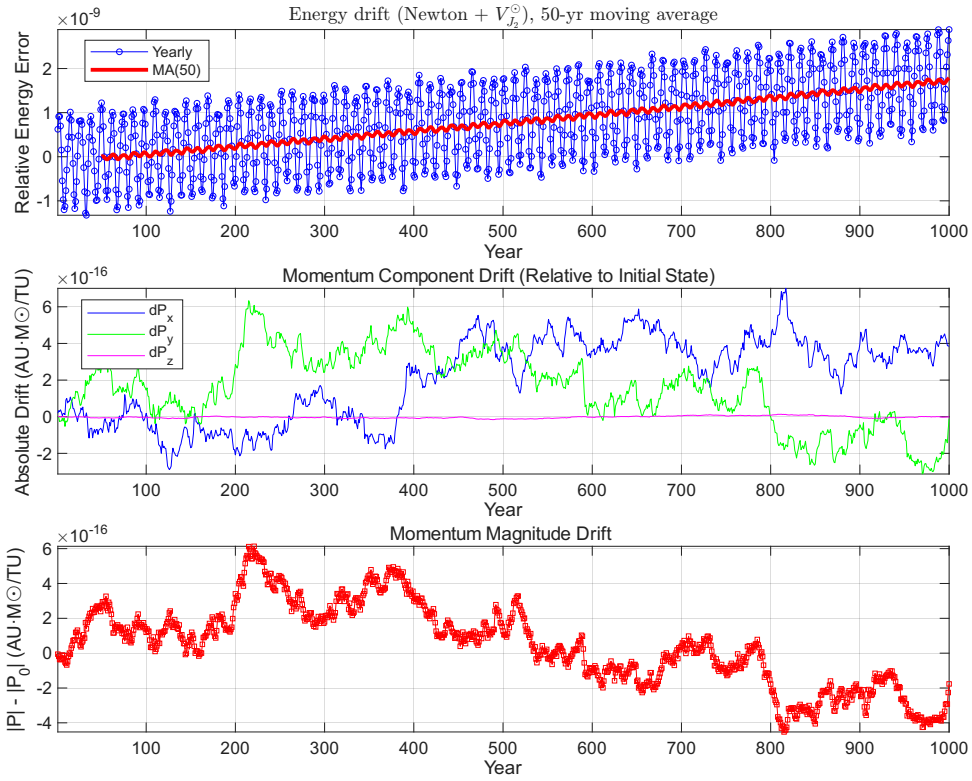


Figure 3: Energy and momentum diagnostics for the constrained 63-stage set in the full model with the 1PN correction activated.

4.5 Step-size dependence

The constrained 63-stage set was also run with macro-steps of 1, 2, 4, and 8 hours for 100 model years. Table 6 reports the endpoint discrepancies relative to DE440. Mercury and Venus display an almost linear dependence on H, consistent with the first-order global contribution predicted by Corollary 1. Earth and Mars approach the same trend at larger steps, while the outer-planet discrepancies are nearly independent of H because the DE440 model offset dominates.

Table 6: Step-size dependence of the 100-year DE440 position discrepancies for the constrained 63-stage scheme.

Body	$H = 1\,\mathrm{h}$	$H = 2\,\mathrm{h}$	$H = 4\,\mathrm{h}$	$H = 8\,\mathrm{h}$
Mercury	1.13×10^{-4}	2.26×10^{-4}	4.51×10^{-4}	9.02×10^{-4}
Venus	3.89×10^{-6}	7.94×10^{-6}	1.60×10^{-5}	3.22×10^{-5}
Earth	1.06×10^{-6}	1.99×10^{-6}	3.87×10^{-6}	7.64×10^{-6}
Moon	2.13×10^{-6}	2.33×10^{-6}	3.77×10^{-6}	7.73×10^{-6}
Mars	3.47×10^{-7}	4.78×10^{-7}	7.64×10^{-7}	1.36×10^{-6}
Jupiter	2.48×10^{-7}	2.49×10^{-7}	2.49×10^{-7}	2.50×10^{-7}
Saturn	1.79×10^{-7}	1.79×10^{-7}	1.79×10^{-7}	1.79×10^{-7}
Uranus	7.26×10^{-7}	7.26×10^{-7}	7.26×10^{-7}	7.26×10^{-7}
Neptune	5.86×10^{-6}	5.86×10^{-6}	5.86×10^{-6}	5.86×10^{-6}
Pluto	6.40×10^{-6}	6.40×10^{-6}	6.40×10^{-6}	6.40×10^{-6}

The table is an external-model check rather than a clean order measurement. A same-model multi-step convergence study for all four coefficient sets would be required to test whether

$$\frac{\|e_w(T;H)\|}{HQ_w}$$

approaches a method-independent limit when the conservative-kernel contribution is negligible.

4.6 Controlled fixed-15-stage family test

As a further controlled test, a 15-stage palindromic family was constructed from positive coefficients by varying a single internal parameter while keeping the stage count, macro-step ($H = 0.5\,\mathrm{h}$), and force-evaluation cost fixed. All coefficients are positive, so $S_3 > 0$ and the family does not cancel conservative moments; it is designed to provide a broad, quasi-continuous range of Q under identical cost and structure. The coefficients are listed in Table 11 in Appendix A.

Thirty members of this family were integrated for 100 model years with the full 28-body model. For each member the complete Mercury endpoint error vector $(\Delta x, \Delta y, \Delta z)$ was recorded. Figure 4 collects the results.

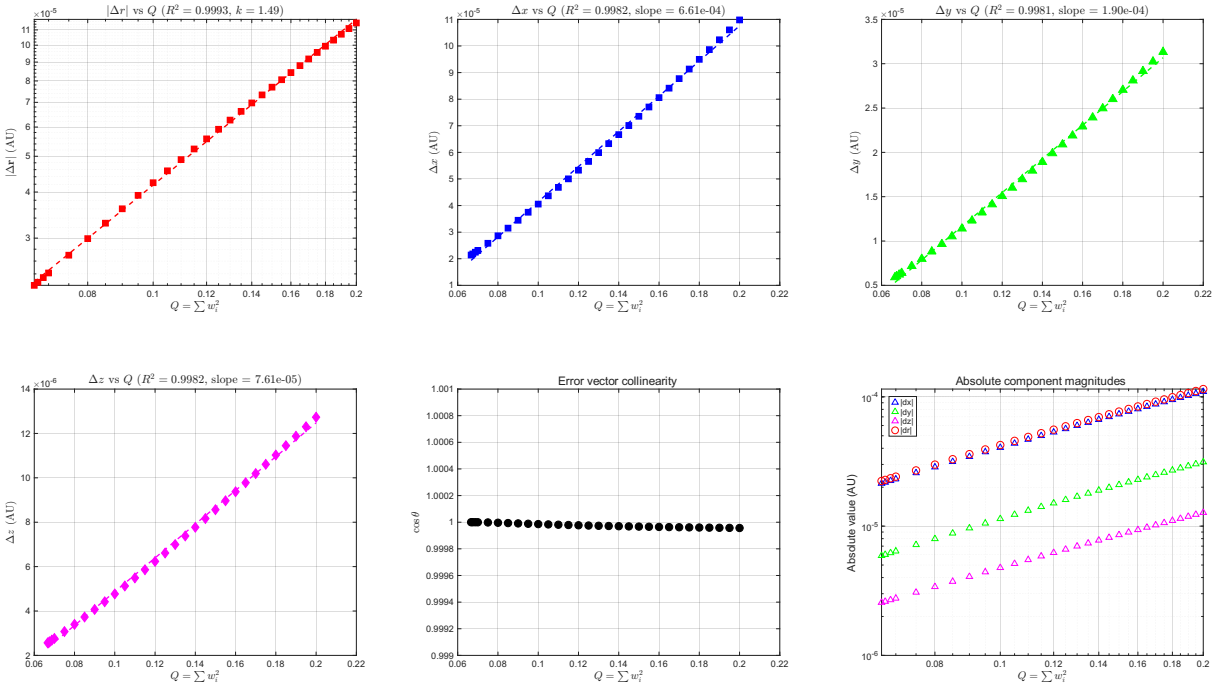


Figure 4: Mercury centennial error for the fixed-15-stage family. (a) Error magnitude $|\Delta\mathbf{r}|$ versus Q with a log-log linear fit ($R^2 = 0.9993$, slope 1.49). (b)–(d) Cartesian components $\Delta x, \Delta y, \Delta z$ versus Q (linear fits, all $R^2 > 0.998$). (e) Cosine of the angle between each member's error vector and that of the minimum-Q member (minimum $\cos\theta = 0.999957$). (f) Absolute component magnitudes in log-log scale.

Across the family, $|\Delta\mathbf{r}|$ scales with Q with $R^2 = 0.9993$ in log-log coordinates, and each Cartesian component individually satisfies a linear relation with $R^2 > 0.998$. Moreover, the error vectors are collinear with the minimum-Q member to within a cosine of 0.999957 (angular deviation $< 0.6°$). The same first-order defect mode is therefore amplified by Q without a detectable change in direction.

The fitted log-log slope of 1.49 is somewhat larger than unity. If the error takes the form $aQ + b$ with $b \neq 0$, the effective log-log slope can deviate from unity. The observed $k = 1.49$ is consistent with a positive a from the velocity-dependent channel and a negative b introduced by the DE440 model offset, which subtracts a constant bias from the total discrepancy. To isolate the role of Q from that of the conservative moments, a second 15-stage family was constructed with the explicit constraint $S_3 = 0$ (enforced to within $|S_3| < 10^{-10}$ by allowing some coefficients to become negative). Thirty members of this constrained family were integrated under identical conditions. The coefficients are listed in Table 12 in Appendix A. The results are shown in Figure 5.

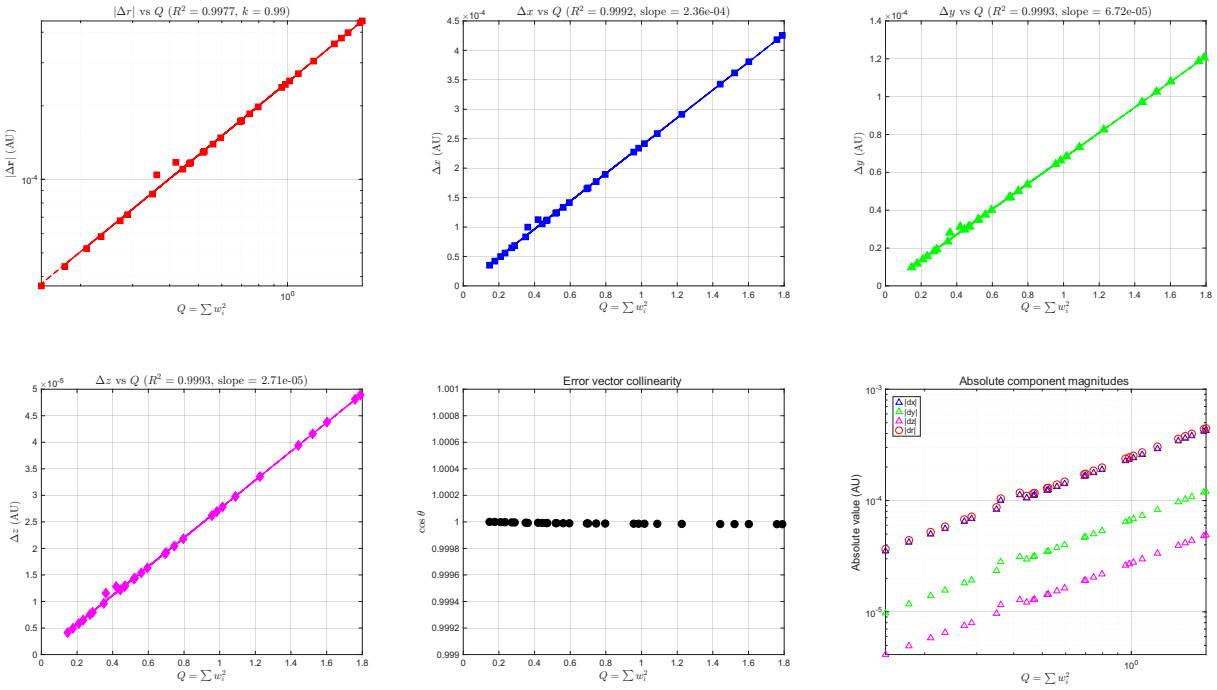


Figure 5: Mercury centennial error for the $S_3 = 0$ constrained 15-stage family. (a) Error magnitude $|\Delta\mathbf{r}|$ versus Q on log-log axes; the fit uses $\log_{10}|\Delta\mathbf{r}|$ versus $\log_{10} Q$ ($R^2 = 0.9977$, slope $k = 0.99$). (b)–(d) Cartesian components $\Delta x, \Delta y, \Delta z$ versus Q on linear axes with linear fits (all $R^2 > 0.999$; reported R^2 values are based on the original linear-scale data). (e) Cosine of the angle between each member's error vector and that of the minimum-Q member (minimum $\cos\theta = 0.99998$). (f) Absolute component magnitudes on log-log axes.

With the conservative moment S_3 removed, the error vector components exhibit excellent linearity with Q ($R^2 > 0.999$ for each Cartesian component), and the error direction remains strictly collinear across the family ($\cos\theta > 0.99998$). The log-log slope of the magnitude is $k = 0.99$, close to unity and consistent with the linear HQ term predicted by Corollary 1 dominating the error budget when the leading conservative contribution is suppressed.

To examine the complementary regime, a third 15-stage family was constructed with Q held fixed at $Q \approx 0.24$ while S_3 was varied by approximately a factor of seven. Thirty members of this fixed-Q family were integrated under the same conditions. The coefficients are listed in Table 13 in Appendix A. The results are shown in Figure 6.

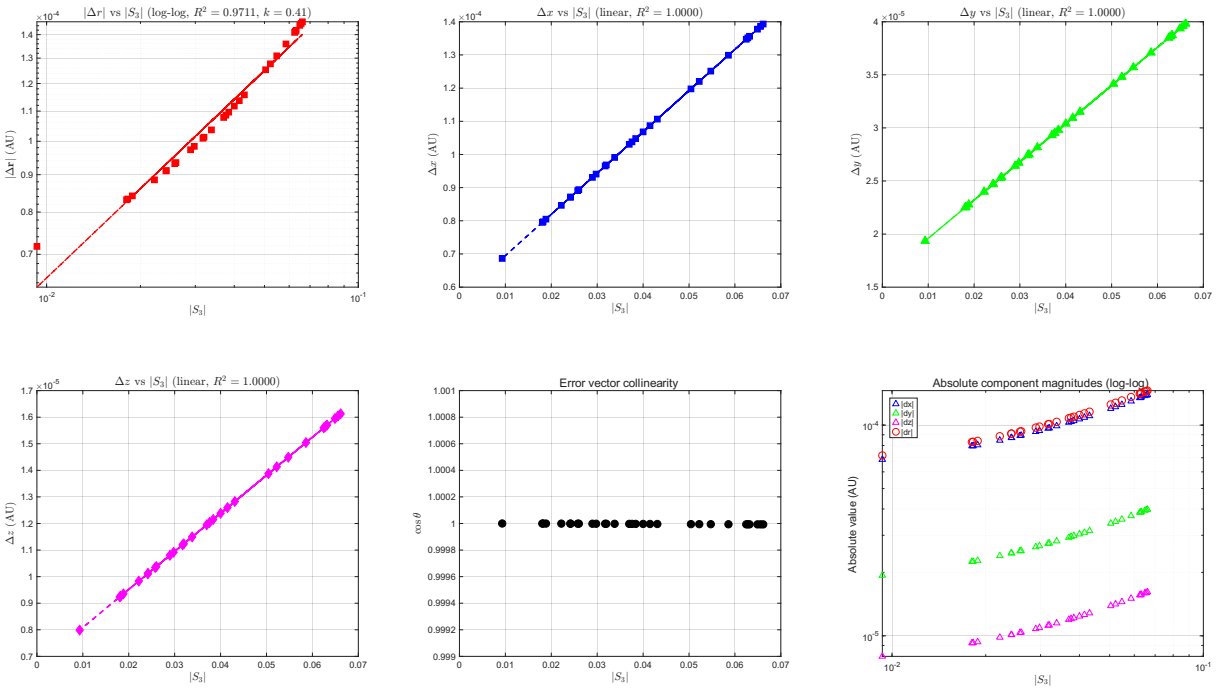


Figure 6: Mercury centennial error for the fixed-Q 15-stage family ($Q \approx 0.24$). (a) Error magnitude $|\Delta\mathbf{r}|$ versus $|S_3|$ on log-log axes ($R^2 = 0.971$, slope $k = 0.41$). (b)–(d) Cartesian components $\Delta x, \Delta y, \Delta z$ versus $|S_3|$ on linear axes with linear fits (all $R^2 = 1.000$). The near-perfect linearity of the components with $|S_3|$ and the non-zero intercepts directly exhibit the two-term error structure $\Delta\mathbf{r} \approx \mathbf{a} + \mathbf{b}|S_3|$, where $\mathbf{a}$ reflects the fixed HQ contribution and $\mathbf{b}|S_3|$ the conservative-kernel contribution. (e) Cosine of the angle between each member's error vector and that of the minimum-$|S_3|$ member (minimum $\cos\theta = 0.99999$). (f) Absolute component magnitudes on log-log axes.

With Q held constant, each Cartesian error component is an essentially perfect linear function of $|S_3|$ (all $R^2 > 0.9999$). The intercepts ($\Delta x_0 = 5.7 \times 10^{-5}$ AU, $\Delta y_0 = 1.6 \times 10^{-5}$ AU, $\Delta z_0 = 6.7 \times 10^{-6}$ AU) correspond to the fixed HQ contribution, while the slopes quantify the conservative-kernel sensitivity. For the equal-step scheme, $S_3 = 1/63^2 \approx 2.52 \times 10^{-4}$. The linear benchmark (Section 4.7) indicates that, under the asymptotic conditions $H = 10^{-4}$ and $\lambda = 0.01$, the S_3-dependent contribution per unit $|S_3|$ is approximately 8.41×10^{-10}. Extrapolating this sensitivity to the Solar System setting would require caution because of the different time scales, step sizes, and model complexity; nevertheless, it illustrates that the bare $H^2 S_3$ term alone is far too small to account for the total error of the equal-step scheme in the one-year same-model test, confirming that higher-order conservative and mixed contributions dominate in that case. This is consistent with the earlier observation that equal steps do not cancel these higher-order terms.

The error vectors remain collinear to within $\cos\theta > 0.99999$, indicating that the Q-dependent and S_3-dependent error modes share essentially the same spatial direction. Taken together, the three 15-stage families provide direct experimental evidence that the total Mercury error vector can be understood as the sum of two independently verifiable contributions: an HQ-scaled velocity-dependent defect and an $H^2 S_3$-scaled conservative-kernel error.

4.7 Exact linear benchmark

To verify the Q-scaling mechanism in a setting free from ephemeris uncertainties and force-model approximations, we apply the same coefficient sets to an anti-damped harmonic oscillator with a linear velocity-dependent term,

$$\dot{q} = p, \qquad \dot{p} = -\omega^2 q + \lambda p, \tag{13}$$

with $\omega = 2\pi$ (unit period) and initial condition $(q_0, p_0) = (1, 0)$. For $\lambda > 0$, the term $+\lambda p$ injects energy and the oscillator is anti-damped. This benchmark is not intended as a physical surrogate for the conservative 1PN dynamics; rather, it supplies an exactly solvable system with $F_p \neq 0$ in which the numerical effect of explicitly evaluated velocity dependence can be isolated. The mathematical structure of the Q-scaling law is independent of the sign of λ. The exact solution is $[q(t), p(t)]^\top = \exp(At)[q_0, p_0]^\top$ with $A = \begin{pmatrix} 0 & 1 \\ -\omega^2 & \lambda \end{pmatrix}$. The relatively large value $\lambda = 0.01$ (compared with the physical 1PN perturbation of $\sim 10^{-8}$) is chosen to make the velocity-dependent defect clearly measurable in double precision; the benchmark validates the mathematical structure of the Q-scaling law rather than the physical magnitude or detailed form of the 1PN effect.

4.7.1 Three-method cross-structure comparison

The linear benchmark is not intended as an independent proof of the asymptotic expansion, but as a controlled verification that isolates the Q-dependent error channel from the competing conservative contributions.

We first compare the equal-step 63-stage, constrained 63-stage, and Morales 35-stage schemes using a macro-step $H = 10^{-4}$ and a total integration time $T = 10$ (ten periods, $N = 10^5$ macro-steps). This small H places the integration well inside the asymptotic regime where the leading HQ term is expected to dominate.

Because $T = 10$ is an integer multiple of the period, the position error alone can be subject to fortuitous cancellations in the conservative limit; we therefore report both the position error $|q(T) - q_{\text{exact}}|$ and the Euclidean norm of the full state error $\|(\Delta q, \Delta p)\|$ as a more robust indicator. Table 7 summarises the results for $\lambda = 0$ and $\lambda = 0.01$.

Table 7: Position errors $|q(T) - q_{\text{exact}}|$ and full state error norms $\|(\Delta q, \Delta p)\|$ for the linear benchmark ($H = 10^{-4}$, $T = 10$, $N = 10^5$ macro-steps). The error ratios quoted in the text are computed from the unrounded data.

Method	Q	S_3	$\lvert q(T) - q_{\text{exact}}\rvert$ ($\lambda = 0$)	$\|(\Delta q, \Delta p)\|$ ($\lambda = 0$)	$\lvert q(T) - q_{\text{exact}}\rvert$ ($\lambda = 0.01$)	$\|(\Delta q, \Delta p)\|$ ($\lambda = 0.01$)
Eq.-step 63	0.0159	2.5×10^{-4}	5.7×10^{-14}	1.6×10^{-9}	1.1×10^{-10}	8.2×10^{-7}
63-stage	0.2269	≈ 0	1.7×10^{-13}	3.0×10^{-12}	1.5×10^{-9}	1.2×10^{-5}
Morales 35	2.9957	≈ 0	1.0×10^{-13}	3.4×10^{-12}	2.0×10^{-8}	1.6×10^{-4}

For $\lambda = 0$ the numerical errors are dominated by round-off and by the conservative truncation terms of each composition; the small position errors reflect special cancellations at the integer-period endpoint and do not represent the true accuracy of the methods. The full state norms reveal that the constrained

63-stage and Morales methods (both with $S_3 \approx 0$) are more accurate than the equal-step scheme by approximately three orders of magnitude, consistent with the conservative order theory. No meaningful ranking can be inferred from the Q values in the purely conservative setting.

For $\lambda = 0.01$ the ranking follows the Q ordering: the equal-step scheme is the most accurate, followed by the 63-stage scheme and the Morales scheme. The error ratios among all three methods, whether computed from the position error or from the full state norm, are in close agreement with their respective Q ratios:

$$\frac{E_{63}}{E_{\text{eq}}} = 14.30, \quad \frac{Q_{63}}{Q_{\text{eq}}} = 14.29 \quad \text{(deviation 0.05\%)};$$
$$\frac{E_{\text{M35}}}{E_{63}} = 13.38, \quad \frac{Q_{\text{M35}}}{Q_{63}} = 13.20 \quad \text{(deviation 1.4\%)};$$
$$\frac{E_{\text{M35}}}{E_{\text{eq}}} = 191.33, \quad \frac{Q_{\text{M35}}}{Q_{\text{eq}}} = 188.73 \quad \text{(deviation 1.4\%)}.$$

The state-norm ratios (14.32, 13.20, 189.13) are consistent with these values to within 0.2%. The close agreement across all three pairwise comparisons confirms that, in the asymptotic regime $H \to 0$ where conservative kernel residuals are fully suppressed, the velocity-dependent error channel scales precisely as HQ, regardless of the specific structure or stage count of the composition.

4.7.2 Continuous Q-scan with the 15-stage $S_3 = 0$ family

To further verify the Q-scaling law with a continuous parameter scan, the 30-member $S_3 = 0$ constrained 15-stage family used in the Solar System test (Section 4.6, Figure 5) was applied to the linear system with $\lambda = 0.01$, using the same small macro-step $H = 10^{-4}$ and total time $T = 10$. The coefficients of this family are provided in Table 12.

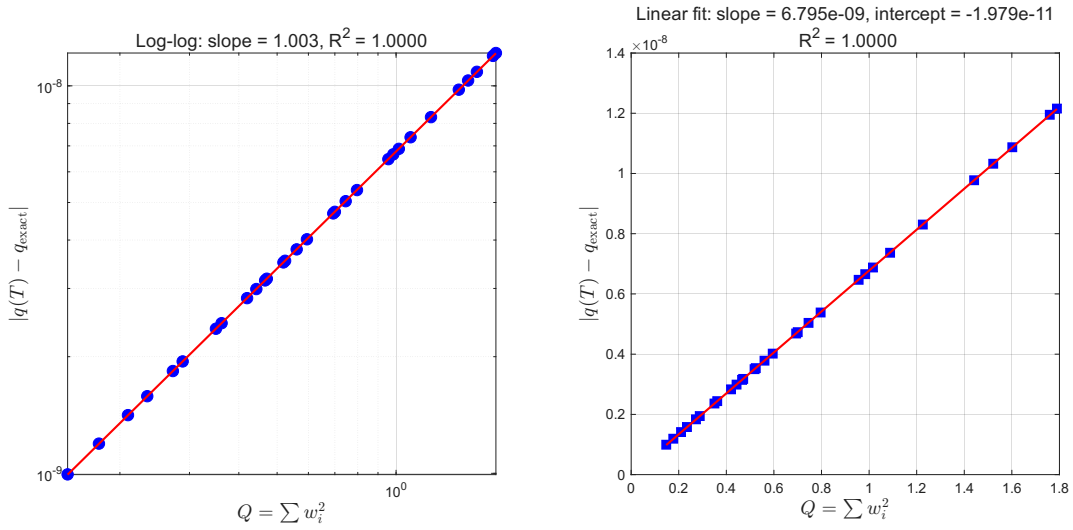


Figure 7: Linear benchmark results for the 30-member $S_3 = 0$ 15-stage family ($\lambda = 0.01$, $H = 10^{-4}$, $T = 10$). (a) Log-log plot: a linear fit yields slope $k = 1.003$ with $R^2 = 0.999999$, confirming the HQ scaling law. (b) Linear plot: the error is an almost perfect linear function of Q ($R^2 = 0.999995$) with slope 6.80×10^{-9} and intercept -1.98×10^{-11}. The near-zero intercept confirms that the S_3-dependent conservative contribution is fully suppressed under the $S_3 = 0$ constraint, leaving the HQ channel as the sole dominant error source.

Figure 7 shows the resulting position errors as a function of Q. In log-log coordinates (panel a), a linear fit gives $R^2 = 0.999999$ and slope $k = 1.003$, in outstanding agreement with the theoretical prediction $k = 1$ from Corollary 1. In linear coordinates (panel b), the error is an almost perfect linear function of Q with $R^2 = 0.999995$, slope 6.80×10^{-9}, and intercept -1.98×10^{-11}. The near-zero intercept is the key signature of the $S_3 = 0$ constraint: without the conservative moment, the $H^2 S_3$ term vanishes, and the total error reduces to the purely Q-dependent HQ channel. This contrasts with the B-family results presented below, where the non-zero intercept directly reflects the fixed HQ contribution.

This 30-point continuous scan provides a direct, high-precision verification of the Q-scaling law under well-controlled, asymptotically clean conditions, and the combination of log-log and linear analyses independently confirms both the scaling exponent ($k \approx 1$) and the absence of a statistically significant residual background.

4.7.3 Separation of the S_3-dependent channel

The complementary regime is examined using the 30-member B-family with fixed $Q \approx 0.24$ and varying S_3 (the same set used in the Solar System test, Figure 6), integrated under identical linear-benchmark conditions ($\lambda = 0.01$, $H = 10^{-4}$, $T = 10$). The coefficients of this family are provided in Table 13. The results are shown in Figure 8.

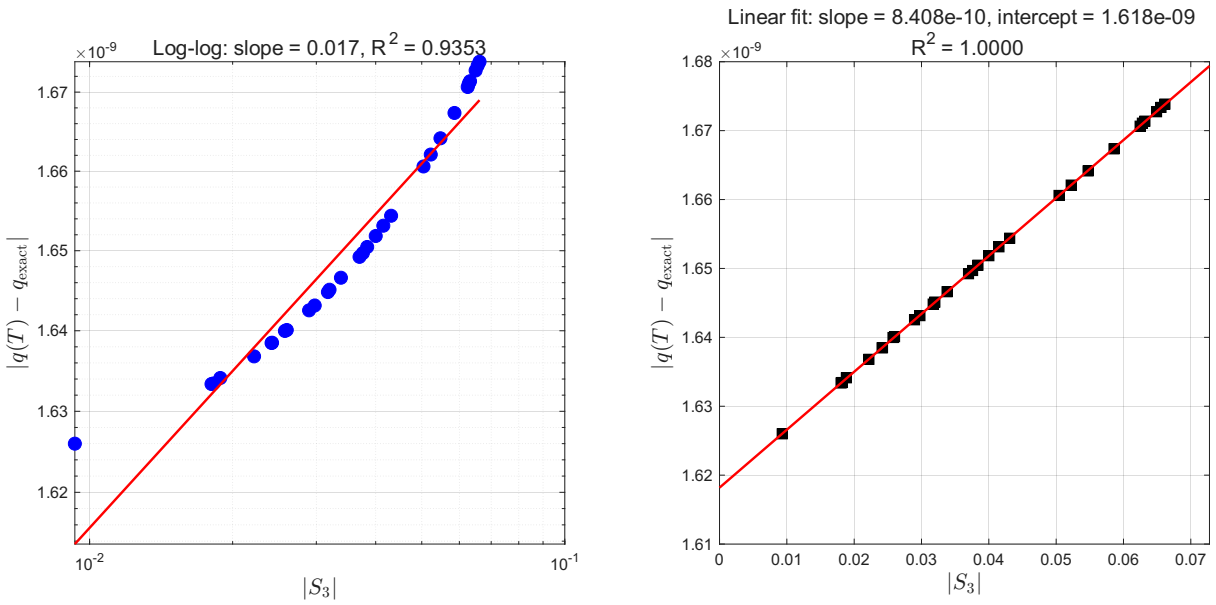


Figure 8: Linear benchmark results for the 30-member fixed-Q B-family ($Q \approx 0.24$, $\lambda = 0.01$, $H = 10^{-4}$, $T = 10$). (a) Log-log plot: the small slope ($k = 0.017$) is a consequence of the non-zero intercept from the HQ term. (b) Linear plot: the error is an almost perfect linear function of $|S_3|$ ($R^2 = 0.999984$), with intercept ($\approx 1.62 \times 10^{-9}$) reflecting the fixed HQ contribution and slope ($\approx 8.41 \times 10^{-10}$ per unit $|S_3|$) quantifying the $H^2 S_3$ sensitivity.

In linear coordinates (Figure 8b), the endpoint error is an almost perfect linear function of $|S_3|$ with $R^2 = 0.999984$. The intercept $\approx 1.62 \times 10^{-9}$ corresponds to the fixed HQ contribution at $Q \approx 0.24$,

while the slope $\approx 8.41 \times 10^{-10}$ per unit $|S_3|$ quantifies the conservative-kernel sensitivity. The non-zero intercepts cause a visible curvature in the log-log representation (Figure 8a), where the fitted slope is only $k = 0.017$—this is exactly the behaviour expected for a two-term error model $\Delta r = a + b|S_3|$ in log-log coordinates, and it provides independent confirmation of the additive structure of the total error.

4.7.4 Summary of the linear-benchmark evidence

Taken together, the linear-benchmark results provide a three-level numerical verification of the Q-scaling law in a fully solvable system:

1. **Cross-structure ratio test:** the error ratios among three structurally different methods agree with their Q ratios to within 1.4% across all pairwise comparisons, with the cleanest pair (63-stage vs. equal-step) showing a deviation of only 0.05% (14.30 vs. 14.29). The same ratios are obtained from the full state norm, confirming that the agreement is not an artefact of the position-only comparison.

2. **Continuous Q-scan:** a 30-point scan under the $S_3 = 0$ constraint yields a log-log slope of $k = 1.003$ with $R^2 = 0.999999$, confirming the linear HQ scaling with high precision.

3. **Channel separation:** a 30-point S_3-scan under fixed Q exhibits near-perfect linearity ($R^2 = 0.999984$) with a non-zero intercept that independently quantifies the HQ contribution, directly exhibiting the two-term error structure $\Delta r \approx \mathbf{a} + \mathbf{b}|S_3|$.

This body of evidence, obtained in a model where the exact solution is known analytically and where the macro-step can be made arbitrarily small without physical constraints, provides a clean numerical confirmation of the theoretical analysis of Section 3.

5 Discussion

The theoretical and numerical results support a more precise conclusion than the statement that "the total error is governed by Q". The explicit velocity-dependent kick creates a distinct first-order error channel whose coefficient is $Q = \sum_i w_i^2$. Proposition 1 and Corollary 1 identify this channel at the local and fixed-time global levels. The one-year same-model experiment then shows that, when the conservative-kernel error is sufficiently suppressed, three very different compositions share the same Q-normalised error constant to within less than one percent for Mercury.

The result is complementary to existing treatments of velocity-dependent or inseparable systems. Algorithmic-regularisation, auxiliary-velocity, specialised splitting, extended-phase-space, and iterative-correction approaches modify the numerical method in order to recover symmetry, higher order, or favourable long-time behaviour [12, 6, 15, 14, 10, 1]. Here the elementary map is deliberately left in the common explicit-kick form, and the objective is instead to identify and quantify the defect inherited by a palindromic coefficient sequence. In this sense, the factor Q is best interpreted as a diagnostic coefficient for an implementation-induced error channel, rather than as a replacement for the general order conditions of composition methods.

The constrained 63-stage and 127-stage sets satisfy $S_3 = 0$ and several additional vanishing power moments, while the Morales set satisfies the full order conditions of a formally 10th-order separable product formula. Their stage counts, coefficient amplitudes, and formal conservative orders are different, yet their one-year Mercury errors follow the reference-corrected quadratic moments almost exactly. This is strong evidence that the explicit 1PN discretisation, rather than the conservative composition order, is the leading error source for these three methods at the tested step.

The equal-step scheme demonstrates the complementary regime. It uniquely minimises Q for $s = 63$, but it is only a repeated second-order Verlet discretisation of the conservative core. At one year, its Mercury error contains substantial uncancelled conservative and mixed $\mathcal{O}(H^2)$ contributions, and the Moon data indicate a markedly different error balance. At 100 years, however, the DE440 comparison is consistent with the much smaller Q producing a large practical advantage for Mercury. The numerical ranking is therefore time-scale- and problem-dependent: it reflects competition between a lower-order perturbation error and higher-order errors, not a universal superiority of equal steps.

The DE440 and same-model tests play different roles. DE440 is an external, observationally fitted ephemeris benchmark and shows whether a change of integrator improves the practical Solar System trajectory. The one-year fine-step reference isolates the discretisation mechanism within the adopted equations. The close agreement of the two lines of evidence is important, but the DE440 discrepancies should not be described as pure truncation errors.

The present comparisons at fixed macro-step are also not cost normalised. They are appropriate for identifying the coefficient mechanism, especially for the equal-cost pair of 63-stage methods, but not for declaring one method globally more efficient than another. The 35-stage and 127-stage methods require substantially different numbers of force evaluations. A separate fixed-cost study would be required for efficiency comparisons.

The long-time energy diagnostics remain useful as structural and implementation checks. Bounded behaviour of the monitored energy in the autonomous conservative control provides a structural check but does not establish the formal order. In the full model, the monitored energy omits both the relativistic and Earth-J_2 contributions, so its secular trend cannot be assigned uniquely to discretisation. Comparative runs with different Q values may still reveal whether part of the drift is numerical, but they must not be used as the primary proof of the Q law.

The local defect formula $-\tau^2 F_p F/4$ derived in Section 3.1 is independent of the specific form of the velocity-dependent force; it applies to any smooth $F(q, p)$ evaluated explicitly in the kick steps. The Q-scaling law is therefore a generic property of palindromic compositions with explicitly treated velocity dependence, not an artefact of the particular 1PN model used in the numerical experiments. The asymptotic result of Proposition 1 is established for a fixed coefficient sequence with bounded $\max_i |w_i|$ as $H \to 0$; its application to families with a wide range of stage numbers should be interpreted as a coefficient-diagnostic tool rather than as a claim of uniform-in-s convergence.

6 Conclusion

An explicit velocity-dependent kick changes the error structure of a palindromically composed Verlet-like method. The elementary map is no longer self-adjoint and has the local momentum defect

$$-\frac{\tau^2}{4} F_p F + \mathcal{O}(\tau^3).$$

A detailed stage-propagation argument shows that the resulting macro-step defect is

$$H^2 Q\, d(y) + \mathcal{O}(H^3), \qquad Q = \sum_i w_i^2,$$

and that the associated fixed-time global contribution is $HQ\,\eta_T + \mathcal{O}(H^2)$.

The one-year same-model Solar System test provides strong evidence consistent with this expansion. After correcting for the nonzero leading defect of the 3-minute reference, the constrained 63-stage, constrained 127-stage, and Morales 35-stage Mercury errors yield Q-normalised constants agreeing within 0.5%. Centennial comparisons with DE440 provide an independent model-consistency indication. Controlled 15-stage families confirm that the Mercury error vector scales linearly with Q for each Cartesian component ($R^2 > 0.998$), and that the error direction remains collinear to within a cosine of 0.99996. An exact linear benchmark further demonstrates the reversal of accuracy ranking between conservative and velocity-dependent regimes, with error ratios consistent with the Q ratios.

Equal steps uniquely minimise Q at fixed stage count, but they do not necessarily minimise the total error. Their conservative-kernel error is not cancelled, and conservative or mixed next-order terms can dominate at shorter times or in rapidly varying subsystems such as the Earth–Moon motion. The appropriate design problem is therefore a balance between the Q-dependent perturbation defect, the conservative composition error, stability, and computational cost.

This study began as an effort to construct a first-principles long-term Solar System integrator. The unexpected inferiority of carefully designed high-order compositions led to the identification of a simple, generic error channel governed by the sum of the squared coefficients. The resulting Q-scaling law explains a large body of numerical observations, is supported by controlled experiments both in a realistic planetary model and in an exactly solvable linear system, and provides a practical guide for choosing composition coefficients whenever velocity-dependent forces must be treated explicitly.

Declarations

Funding. This work was supported by no funding.

Author Contribution. Jiaqi Shen is the sole author. He conceived the study, performed the theoretical analysis, designed and carried out the numerical experiments, and wrote the manuscript.

Appendix A Composition coefficients

The full 63-stage sequence is

$$(x_1, \ldots, x_{31}, x_{32}, x_{31}, \ldots, x_1),$$

and the full 127-stage sequence is defined analogously from $x_1, \ldots, x_{64}$. The Morales sequence is

$$(x_1, \ldots, x_{17}, x_{18}, x_{17}, \ldots, x_1), \qquad x_{18} = 1 - 2\sum_{j=1}^{17} x_j.$$

The production calculations used the internally stored coefficient values; the decimal values below are rounded to 15 digits.

Table 8: The 32 independent parameters of the 63-stage palindromic composition.

$x_1 \ldots x_8$	$x_9 \ldots x_{16}$	$x_{17} \ldots x_{24}$	$x_{25} \ldots x_{32}$
0.023060973920552	0.023061015593888	0.023061044902071	0.023060961658261
0.023061107243115	0.023060939353201	-0.156876007589772	0.023061063773437
0.023061084454041	0.023061038047659	0.023061106526816	0.023061013415349
0.023061050340888	0.023061085931821	0.023061118737562	0.023061106774835
0.023061099168960	0.128141084114530	-0.077524191598979	0.023061128974555
0.023061099699958	0.023060986842251	0.023061164352456	0.023061104849981
0.023061087954124	0.023061181658302	0.023061072263035	0.023061170424616
0.023061032997032	-0.077524277596172	0.174227031010522	-0.180062956397789

Table 9: The 64 independent parameters of the exploratory 127-stage palindromic composition. The full set contains 127 elements through palindromic symmetry.

$x_1 \ldots x_8$	$x_9 \ldots x_{16}$	$x_{17} \ldots x_{24}$	$x_{25} \ldots x_{32}$
0.014496632595367	0.014497036389637	0.014607343719958	0.094333149532245
0.014496612899699	0.014493700805872	0.013984565203216	0.088428313747284
0.014496718040833	0.014495258704301	0.014044260669385	0.027864989616280
0.014496801348043	0.014507641861782	0.016302860227662	0.011232956916832
0.014496720598016	0.014503050257428	0.016288253346061	0.019006792875365
0.014496456640030	0.014457227593218	0.007410955999988	-0.015394712513764
0.014496616483758	0.014469887943190	0.006566557326654	-0.082618145249433
0.014497528748364	0.014638578776086	0.052343064725775	-0.058669521835359
$x_{33} \ldots x_{40}$	$x_{41} \ldots x_{48}$	$x_{49} \ldots x_{56}$	$x_{57} \ldots x_{64}$
0.010296731566581	-0.069497390197699	0.082909602510798	0.015189776418855
-0.020436604245595	-0.075863020110520	0.006292787068800	0.014334698425968
-0.125321509157445	-0.018079232749712	0.001408262042250	0.012684820144318
-0.157067569394880	0.016445210863180	0.016239013069466	0.014848050102825
-0.050121090252749	0.006195623422318	0.017510569709452	0.020767690387154
0.035176844342157	0.027594385006939	0.014073743297977	0.013857344639547
0.038227228156654	0.144659589211209	0.013527479925963	-0.049608466132606
-0.009516816671268	0.159219675005957	0.014638000982302	-0.156707162763934

Table 10: The 17 outer coefficients $x_1, \ldots, x_{17}$ and the central coefficient x_{18} of the Morales 35-stage set, reproduced from Table III of [13].

$x_1 \ldots x_6$	$x_7 \ldots x_{12}$	$x_{13} \ldots x_{18}$
0.104377427795478	0.431999356095233	−0.531231343926807
0.121184694986507	−0.305839818355735	0.191862040946745
0.150439369438172	0.538358469475468	0.368458923827978
0.103297112584429	0.185147661192914	0.046779504778147
−0.350510992048297	−0.163894504143786	−0.283712326891443
0.151050230163179	−0.008125324272083	−0.499280963292202

Table 11: Coefficients of the positive 15-stage family (ordered by increasing Q). The full 15-weight sequence is obtained by palindromic symmetry as $w = (x_1, \ldots, x_7, x_8, x_7, \ldots, x_1)$.

Member	x_1	x_2	x_3	x_4	x_5	x_6	x_7	x_8	Q
1	0.066667	0.066667	0.066667	0.066667	0.066667	0.066667	0.066667	0.066667	0.0667
2	0.083779	0.071681	0.065368	0.062699	0.061857	0.061755	0.061866	0.061988	0.0675
3	0.093724	0.074595	0.064614	0.060394	0.059063	0.058900	0.059076	0.059269	0.0688
4	0.100892	0.076695	0.064070	0.058732	0.057048	0.056843	0.057065	0.057310	0.0700
5	0.120782	0.082524	0.062561	0.054120	0.051459	0.051134	0.051485	0.051872	0.0750
6	0.135118	0.086724	0.061473	0.050797	0.047430	0.047019	0.047463	0.047953	0.0800
7	0.146933	0.090186	0.060577	0.048058	0.044110	0.043627	0.044148	0.044723	0.0850
8	0.157219	0.093200	0.059797	0.045673	0.041219	0.040675	0.041262	0.041911	0.0900
9	0.166450	0.095905	0.059096	0.043532	0.038625	0.038025	0.038672	0.039387	0.0950
10	0.174897	0.098380	0.058455	0.041574	0.036251	0.035600	0.036303	0.037078	0.1000
11	0.182731	0.100676	0.057861	0.039758	0.034049	0.033352	0.034105	0.034936	0.1050
12	0.190069	0.102826	0.057304	0.038057	0.031987	0.031246	0.032046	0.032930	0.1100
13	0.196994	0.104855	0.056779	0.036451	0.030041	0.029258	0.030104	0.031037	0.1150
14	0.203569	0.106782	0.056280	0.034927	0.028193	0.027371	0.028259	0.029239	0.1200
15	0.209842	0.108620	0.055804	0.033472	0.026430	0.025570	0.026499	0.027524	0.1250
16	0.215852	0.110381	0.055348	0.032079	0.024741	0.023845	0.024813	0.025881	0.1300
17	0.221629	0.112074	0.054910	0.030740	0.023118	0.022187	0.023192	0.024302	0.1350
18	0.227199	0.113706	0.054487	0.029448	0.021553	0.020588	0.021630	0.022779	0.1400
19	0.232581	0.115283	0.054079	0.028200	0.020040	0.019043	0.020119	0.021308	0.1450
20	0.237794	0.116810	0.053684	0.026992	0.018575	0.017547	0.018657	0.019883	0.1500
21	0.242853	0.118293	0.053300	0.025819	0.017153	0.016095	0.017238	0.018500	0.1550
22	0.247771	0.119734	0.052927	0.024679	0.015771	0.014683	0.015858	0.017155	0.1600
23	0.252559	0.121137	0.052563	0.023569	0.014426	0.013309	0.014515	0.015846	0.1650
24	0.257226	0.122504	0.052209	0.022487	0.013114	0.011969	0.013205	0.014570	0.1700
25	0.261782	0.123839	0.051864	0.021430	0.011834	0.010661	0.011927	0.013325	0.1750
26	0.266234	0.125144	0.051526	0.020398	0.010582	0.009383	0.010678	0.012108	0.1800
27	0.270589	0.126420	0.051196	0.019389	0.009359	0.008133	0.009456	0.010917	0.1850
28	0.274853	0.127669	0.050872	0.018400	0.008160	0.006910	0.008260	0.009751	0.1900
29	0.279031	0.128893	0.050555	0.017431	0.006986	0.005710	0.007088	0.008609	0.1950
30	0.283128	0.130094	0.050244	0.016482	0.005835	0.004534	0.005939	0.007489	0.2000

Table 12: Coefficients of the $S_3 = 0$ 15-stage family (ordered by increasing Q). The full 15-weight sequence is obtained by palindromic symmetry as $w = (x_1, \ldots, x_7, x_8, x_7, \ldots, x_1)$.

Member	x_1	x_2	x_3	x_4	x_5	x_6	x_7	x_8	Q
1	0.086282	0.086283	0.086282	0.086282	0.086282	0.086282	0.086282	−0.207953	0.1475
2	0.097845	0.096716	0.131111	0.095837	0.029266	0.106469	0.059848	−0.234187	0.1770
3	0.066353	0.156606	0.056889	0.136687	0.101980	0.014831	0.096938	−0.260567	0.2096
4	0.110151	0.110148	0.110150	0.110155	0.110153	0.110149	−0.202529	0.083247	0.2346
5	0.168334	−0.023855	0.033962	0.128759	0.169602	0.109877	0.062891	−0.299139	0.2723
6	0.084448	−0.230425	0.170240	0.107152	0.140838	0.077231	0.129613	0.041806	0.2883
7	0.141103	0.261429	−0.004747	0.028304	0.076370	0.109246	0.066787	−0.356983	0.3500
8	0.064341	0.067979	0.206328	0.165031	0.197251	0.016882	−0.042750	−0.350123	0.3618
9	0.192233	0.165892	−0.219972	0.090713	0.141366	0.124045	0.137180	−0.262915	0.4197
10	0.184488	0.074934	0.020609	0.278970	0.148965	−0.034775	0.026184	−0.398749	0.4430
11	0.102814	0.207997	0.004784	0.030837	−0.080608	0.241932	0.189096	−0.393707	0.4662
12	0.172785	0.077729	0.195812	−0.255947	0.098793	0.140506	0.191686	−0.242729	0.4709
13	0.117750	0.262793	0.077690	0.141447	0.223135	0.022589	−0.147530	−0.395748	0.5187
14	0.274887	0.048340	−0.327194	0.082285	0.099136	0.091416	0.227973	0.006312	0.5238
15	−0.324153	0.205697	0.003237	0.164381	0.066329	0.201584	0.235142	−0.104434	0.5604
16	−0.113773	0.117187	−0.326051	0.243419	0.209582	0.190930	0.084632	0.188148	0.5950
17	−0.367615	−0.076160	0.171387	0.027423	0.303189	0.144884	0.161392	0.271001	0.6935
18	−0.323562	0.208651	0.169094	0.217296	0.242837	0.100641	−0.203265	0.176617	0.7001
19	0.223224	−0.179453	0.188153	0.136548	0.006515	0.019838	0.346334	−0.482318	0.7456
20	0.202836	0.096366	0.039828	0.309265	−0.129753	0.312195	−0.075258	−0.510959	0.7963
21	−0.067277	−0.433839	0.380683	−0.066676	0.210595	0.190396	0.206912	0.158413	0.9561
22	0.249541	0.149981	0.292089	−0.407646	0.005974	0.295482	−0.202351	0.233862	0.9838
23	0.190295	0.207301	0.223318	−0.457661	−0.120997	0.062730	0.138123	0.513780	1.0163
24	−0.097481	0.333783	0.324355	0.256306	0.171544	−0.298815	0.064711	−0.508804	1.0883
25	0.373960	0.159912	−0.484060	−0.187750	0.231001	0.121602	0.054236	0.462201	1.2258
26	0.356367	−0.469896	0.397194	0.062591	0.231082	−0.314368	0.242824	−0.011589	1.4415
27	0.379232	−0.236834	0.137713	0.431515	0.293244	0.056849	−0.237595	−0.648249	1.5217
28	0.054708	−0.021210	0.276647	−0.055092	−0.234589	0.299255	0.549004	−0.737447	1.6018
29	0.363496	0.067357	0.365379	0.248921	−0.540919	−0.324657	0.049170	0.542507	1.7594
30	−0.627458	0.212913	0.167515	0.147612	0.286489	0.113497	−0.174916	0.748696	1.7894

Table 13: Coefficients of the fixed-Q ($Q \approx 0.24$) 15-stage family (ordered by increasing S_3). The full 15-weight sequence is obtained by palindromic symmetry as $w = (x_1, \ldots, x_7, x_8, x_7, \ldots, x_1)$.

Member	x_1	x_2	x_3	x_4	x_5	x_6	x_7	x_8	S_3
1	0.129615	−0.186746	0.160944	0.128902	0.079907	0.124241	0.063135	0.000000	0.009311
2	0.086479	0.178001	0.078512	−0.170306	0.039910	0.106450	0.180953	0.000000	0.018052
3	0.156407	0.006786	−0.165750	0.178552	0.128150	0.114282	0.081572	0.000000	0.018210
4	−0.167496	0.163496	0.077986	0.053059	0.152131	0.044112	0.176712	−0.000000	0.018840
5	0.088372	0.012133	0.059429	0.160420	−0.158080	0.188332	0.149394	−0.000000	0.022188
6	0.223848	0.106918	0.020252	0.112479	0.121745	0.073448	−0.158690	−0.000000	0.024149
7	0.095629	0.100465	0.104593	−0.152084	0.151850	0.208688	−0.009141	0.000000	0.024208
8	0.094456	0.181415	0.158318	0.080256	−0.038815	−0.137577	0.161949	−0.000000	0.025767
9	0.153829	0.065614	−0.005905	−0.146806	0.163744	0.074301	0.195222	0.000000	0.025998
10	0.209249	0.108840	−0.138243	0.177396	−0.020460	0.086586	0.076630	−0.000000	0.028965
11	0.082646	−0.144293	0.093730	0.223175	0.062138	0.009988	0.172615	0.000000	0.029767
12	0.059126	−0.140499	0.006107	0.115634	0.145262	0.077060	0.237311	−0.000000	0.031734
13	−0.145118	0.247272	0.126732	0.023860	0.077593	0.065416	0.104244	0.000000	0.031984
14	0.180597	−0.049274	0.091630	−0.107445	0.169892	0.188314	0.026286	−0.000000	0.033799
15	0.065987	0.247410	0.135417	−0.123364	−0.015273	0.131161	0.058662	0.000000	0.036984
16	0.158101	0.117301	0.115946	0.233793	−0.050298	0.025074	−0.099917	−0.000000	0.037589
17	0.246293	0.091146	0.099738	−0.071335	0.079130	0.146300	−0.091272	−0.000000	0.038386
18	0.051182	0.151570	0.009136	−0.103649	0.174512	−0.012881	0.230131	0.000000	0.040007
19	−0.056911	0.176485	0.130228	0.229510	−0.044311	−0.044650	0.109650	0.000000	0.041506
20	−0.046386	−0.030670	0.082401	−0.059629	0.157101	0.159836	0.237347	−0.000000	0.043101
21	0.004005	0.266673	0.003328	−0.080642	0.090220	0.034730	0.181685	0.000000	0.050427
22	0.208883	0.063978	−0.057329	0.048728	0.256307	0.008545	−0.029112	0.000000	0.052233
23	0.108143	−0.022878	−0.061533	0.080189	0.289366	0.117148	−0.010435	−0.000000	0.054743
24	−0.014797	0.067562	−0.047870	0.295441	0.144109	0.068577	−0.013021	−0.000000	0.058592
25	−0.049255	0.043962	0.309309	0.105037	−0.031138	0.045008	0.077077	−0.000000	0.062471
26	−0.022749	0.006433	0.297580	0.030962	−0.007082	0.023624	0.171232	0.000000	0.062807
27	−0.014690	0.071158	0.027052	0.311856	0.081638	0.081514	−0.058528	−0.000000	0.063183
28	0.093810	0.083328	−0.018277	−0.018977	−0.023176	0.313236	0.070056	0.000000	0.064913
29	0.075042	0.022291	−0.063943	0.059630	0.018663	0.317617	0.070699	−0.000000	0.065571
30	−0.002731	0.315510	−0.040615	0.027198	0.012163	0.102819	0.085657	0.000001	0.066156

The coefficients in Table 11, Table 12, and Table 13 are rounded to six decimal places for compact presentation. All numerical integrations and reported coefficient moments were evaluated using the original full-precision values.

Appendix B Extended energy diagnostics

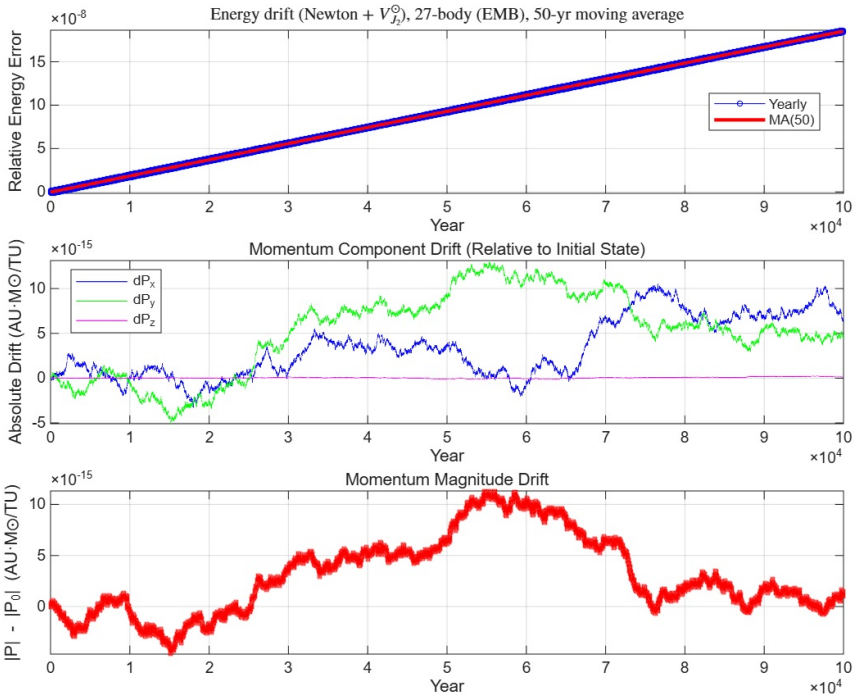


Figure 9: Energy and momentum diagnostics over 100,000 model years for the full model, monitored on the 27-body Earth–Moon-barycentre (EMB) representation. The monitored-energy trend persists with a nearly constant slope. This diagnostic provides a long-interval implementation check but does not directly validate the Q-scaling law, because it uses a single coefficient set and a barycentre-merged diagnostic that is not a direct continuation of the 28-body series.

References

[1] Akramov, I., Götschel, S., Minion, M., Ruprecht, D., Speck, R.: Spectral deferred correction methods for second-order problems. SIAM J. Sci. Comput. 46, A1690–A1713 (2024). doi:10.1137/23M1592596

[2] Blanes, S., Casas, F., Murua, A.: Composition methods for differential equations with processing. SIAM J. Sci. Comput. 27, 1817–1843 (2006). doi:10.1137/030601223

[3] Park, R.S., Folkner, W.M., Williams, J.G., Boggs, D.H.: The JPL Planetary and Lunar Ephemerides DE440 and DE441. Astron. J. 161, 105 (2021). doi:10.3847/1538-3881/abd414

[4] Hairer, E., Lubich, C., Wanner, G.: Geometric Numerical Integration: Structure-Preserving Algorithms for Ordinary Differential Equations, 2nd edn. Springer, Berlin (2006)

[5] Hairer, E., Nørsett, S.P., Wanner, G.: Solving Ordinary Differential Equations I: Nonstiff Problems, 2nd revised edn. Springer, Berlin (1993)

[6] Hellström, C., Mikkola, S.: Explicit algorithmic regularization in the few-body problem for velocity-dependent perturbations. Celest. Mech. Dyn. Astron. 106, 143–156 (2010). doi:10.1007/s10569-009-9248-8

[7] Giorgini, J.D., Yeomans, D.K., Chamberlin, A.B., Chodas, P.W., Jacobson, R.A., Keesey, M.S., Lieske, J.H., Ostro, S.J., Standish, E.M., Wimberly, R.N.: JPL's On-Line Solar System Data Service. Bull. Am. Astron. Soc. 28, 1158 (1996)

[8] Laskar, J.: A numerical experiment on the chaotic behaviour of the Solar System. Nature 338, 237–238 (1989). doi:10.1038/338237a0

[9] Laskar, J., Robutel, P., Joutel, F., Gastineau, M., Correia, A.C.M., Levrard, B.: A long-term numerical solution for the insolation quantities of the Earth. Astron. Astrophys. 428, 261–285 (2004). doi:10.1051/0004-6361:20041335

[10] Liu, L., Wu, X., Huang, G., Liu, F.: Higher order explicit symmetric integrators for inseparable forms of coordinates and momenta. Mon. Not. R. Astron. Soc. 459, 1968–1976 (2016). doi:10.1093/mnras/stw807

[11] McLachlan, R.I.: On the numerical integration of ordinary differential equations by symmetric composition methods. SIAM J. Sci. Comput. 16, 151–168 (1995). doi:10.1137/0916010

[12] Mikkola, S., Merritt, D.: Algorithmic regularization with velocity-dependent forces. Mon. Not. R. Astron. Soc. 372, 219–223 (2006). doi:10.1111/j.1365-2966.2006.10854.x

[13] Morales, M.E.S., Costa, P.C.S., Pantaleoni, G., Burgarth, D.K., Sanders, Y.R., Berry, D.W.: Selection and improvement of product formulae for best performance of quantum simulation. Quantum Inf. Comput. 25, 1–35 (2025). doi:10.2478/qic-2025-0001

[14] Pihajoki, P.: Explicit methods in extended phase space for inseparable Hamiltonian problems. Celest. Mech. Dyn. Astron. 121, 211–231 (2015). doi:10.1007/s10569-014-9597-9

[15] Rein, H., Tremaine, S.: Symplectic integrators in the shearing sheet. Mon. Not. R. Astron. Soc. 415, 3168–3176 (2011). doi:10.1111/j.1365-2966.2011.18939.x

[16] Robertson, H.P.: Dynamical effects of radiation in the Solar System. Mon. Not. R. Astron. Soc. 97, 423–437 (1937). doi:10.1093/mnras/97.6.423

[17] Saha, P., Tremaine, S.: Long-term planetary integration with individual time steps. Astron. J. 108, 1962–1969 (1994). doi:10.1086/117210

[18] Suzuki, M.: General theory of higher-order decomposition of exponential operators and symplectic integrators. Phys. Lett. A 165, 387–395 (1992). doi:10.1016/0375-9601(92)90335-J

[19] Will, C.M.: The confrontation between general relativity and experiment. Living Rev. Relativ. 17, 4 (2014). doi:10.12942/lrr-2014-4

[20] Wisdom, J., Holman, M.: Symplectic maps for the N-body problem. Astron. J. 102, 1528–1538 (1991). doi:10.1086/115978

[21] Yoshida, H.: Construction of higher order symplectic integrators. Phys. Lett. A 150, 262–268 (1990). doi:10.1016/0375-9601(90)90092-3